Hydrological, Geochemical, and Microbiological Controls on Iron Mineralization in an Intermittent Stream

Zackry Stevenson[1], Mia Riddley[1], Tamara McConnell[1], Elizabeth D. Swanner[1*]

[1]Iowa State University, Department of Geological and Atmospheric Sciences, Ames, IA, USA

*** Correspondence:**

Elizabeth D. Swanner

eswanner@iastate.edu

Abstract

In Clear Creek, which runs through the Iowa State University campus in Ames, Iowa, U.S.A., several types of iron mineralization occur within stagnant pools and slow-moving water. This includes rusty flocs, commonly observed in mineral springs, rust-stained sediments, and iridescent films ("schwimmeisen") on the pool surfaces. Observations of iron mineralization over the course of more than a year in a single reach indicated that mineralization occurred after precipitation events, once water levels in the stream had dropped. Iron extracted and quantified from Clear Creek sediments and pool waters indicated the stream and its sediments were unlikely to be supplying the iron for mineralization. We hypothesize that the observed mineralization could result from the discharge of shallow, reducing, groundwater-bearing Fe(II) into stagnant pools that form in debris-dammed areas of the stream. Piezometers installed next to the creek documented that shallow groundwater contained dissolved Fe, with the source of Fe being the floodplain sediments, and the hydraulic gradient promoted groundwater discharge into the stream. Microorganisms identified in mineralized pools using 16S rRNA amplicon sequencing revealed an elevated presence of putative iron-oxidizing and iron-reducing microorganisms in mineralized vs. non-mineralized pools. Further investigation of the iridescent films revealed them to be composed of amorphous Fe(III) minerals. We further hypothesize that microbial exudates reduce surface tension and potential micro-zones for subsequent microbial iron redox cycling with dissolved organic matter in the pools. Determining the processes controlling mineralization can lead to a better understanding of the ecological role of iron mineralization in agricultural watersheds, and the importance in contaminant degradation and nutrient cycling.

Introduction

Streams are important conduits of elements between watersheds, downstream rivers, or estuaries. A stream's chemical inputs reflect the local watershed characteristics. Specifically, the hyporheic zone is influenced by groundwater quality and neighboring ecosystems that impact the cycling of nitrogen, phosphorus, and sulfur (Lawrence et al., 2013). Agricultural watersheds with forested riparian zones can enhance nitrogen and phosphorus cycling through biotic uptake, sediment deposition, agricultural runoff, and seasonal dynamics (Kreiling et al., 2021). However, there is less work to address the hydrology and biogeochemistry of iron cycling in lower-order agricultural streams. Slow-moving water contributes to intermittent suspended organic material deposition, which aids in the development and maintenance of oxygen gradients in water and sediment porewaters, which can alter the mobility of iron and other redox-active trace metals

(Rosenburg & Schroth, 2017). In particular, the hyporheic zone in these streams is an interface between the anoxic and/or trace-metal-rich groundwater, with an oxidative and reductive capacity that can affect elemental cycling (Boano et al., 2014; Hoagland et al., 2020; Yang et al., 2018), including iron redox cycling (Boulton et al., 1998). Determining where and how iron enters such streams is important to identify hot spots of microbial iron and nutrient cycling, which can drive contaminant degradation or immobilization through processes such as adsorption onto iron minerals. This is particularly important for agricultural watersheds or those with other disturbances that affect water quality and ecology.

Iron is present in Earth's surface environment as a major crustal cation, as oxides during weathering, as an ion dissolved in water, and within biological organisms as a requisite trace nutrient. Iron moves between these different reservoirs when it is transformed between its primary oxidation states (i.e., Fe(II) and Fe(III)) and distinct chemical species, which control the solubility and mobility of iron (Kappler et al., 2021). Seeps and springs where anoxic groundwater discharges to the oxygenated surface are hot spots for microbial redox cycling and iron mineralization at such sites have previously been observed (Kozubal et al., 2008; Mori et al., 2015; Pierson & Parenteau, 2000). Several possibilities for iron inputs exist for creek beds and streams, including iron mobilization within the riparian zone, from the hyporheic zone, during shallow or deep groundwater discharge, or inputs from the larger watershed during rain events (Lautz & Fanelli, 2008; Rivett et al., 2011; Sarkkola et al., 2013). Two other common iron sources are from acid rock drainage, where iron sulfides are weathered (Ahn et al., 2015; Dold et al., 2013), or through acid mine drainage in mine-impacted areas (Méndez-García et al., 2015).

Seeps and springs can introduce Fe(II) from anoxic groundwater, utilized by iron-oxidizing organisms as it discharges into oxygenated water. Iron-oxidizing bacteria (FeOB) can oxidize Fe(II) to Fe(III) under both oxic and anoxic aquatic conditions and have previously been recognized as contributing to in-creek iron deposits (Emerson, 2012; Roden et al., 2012). Freshwater environments with circumneutral pH are generally dominated by FeOB within the *Gallionellaceae* family (G*allionella capsiferriformans*) (Almaraz et al., 2017; Roden et al., 2012). In contrast, *Sideroxydans* sp. are FeOB found in acidic and circumneutral environments (Fabisch et al., 2013; Roden et al., 2012). Moreover, these FeOB make up flocculent iron mats in various freshwater systems (Brooks and Field, 2020). In circumneutral pH and oxygenated conditions, Fe(III) is the favored valence, which is relatively insoluble and forms Fe(III)-(oxyhydr)oxides (Cornell et al., 1996; Sobolev & Roden, 2002). *Acidithiobacillus* and *Lepstospirillum* have been found in acidic streams and are known FeOB that contribute heavily to the iron oxidation in these systems (Méndez-García et al., 2015). Variations in pH, nutrients, oxygen content, and organic matter inputs can control the identity and compositions of Fe(III)-(oxyhydr)oxide minerals, which then provide electron sources for various iron-respiring organisms (Bruun et al., 2010; Chan et al., 2016; Emerson et al., 2010; Roden et al., 2012). Oxygen-poor conditions could result from water stagnation and particulate organic carbon input, allowing iron-reducing bacteria (FeRB) to reductively dissolve mineralized Fe(III) (Brooks and Field, 2020; Dubinsky et al., 2010; Lovley, 1987). Floating surface films of iron have been detected in multiple seeps, springs, and creeks, and could be a hotspot for microbial activity (Almaraz et al., 2017; Dong et al., 2024; Grathoff et al., 2007; Sánchez-España et al., 2023). However, the oxidation state and mineralogy of floating iron films are not well-characterized, and there is conflicting evidence on whether these formations are Fe(II), Fe(III), or a mixture of

both (Dong et al., 2024; Grathoff et al., 2007; Perkins et al., 2016). Furthermore, there is little comparative work on the microbial community composition associated with floating iron films vs. flocculant iron mats or other types of in-creek iron mineralization.

This study reports observations of iron mineralization in an intermittent stream located in Ames, IA, U.S.A., to provide a combined hydrological, geochemical, and microbiological investigation of iron sources and microbial redox cycling. This stream is of particular interest because it is in an agricultural watershed, and iron-cycling organisms can play a role in organic pollutant (e.g., herbicide) degradation, or nutrient cycling. Our goals were to (1) inform the source of iron to the stream, (2) document the geochemical conditions that give rise to the observed iron deposits, (3) investigate the microorganisms associated with the iron mineralization types, and (4), resolve the oxidation state and mineralogy of iron in floating iron films. These results will elucidate the impact of hydrology, geochemistry, and microbiology on in-stream iron cycling and mineralization.

Methods

Field Description

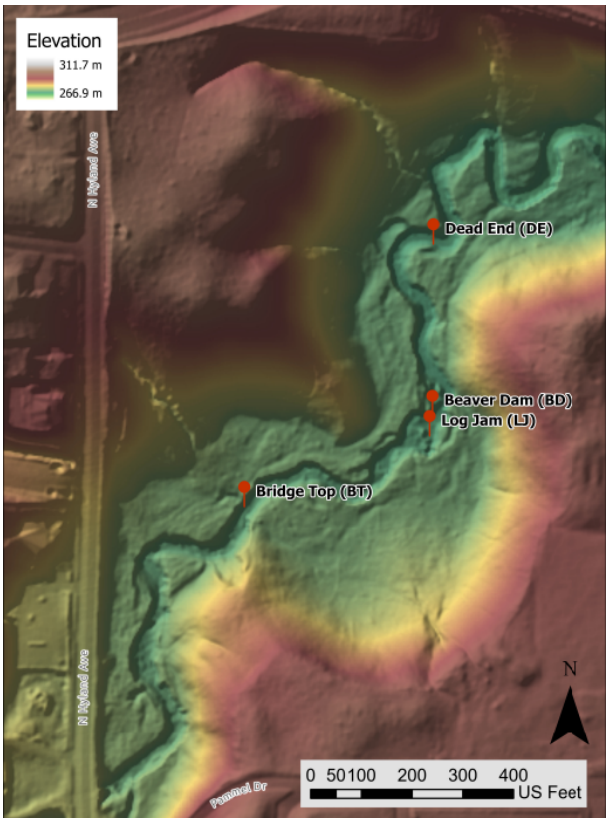

Figure 1: LiDAR map of Clear Creek on Iowa State University's campus in Ames, IA, produced in ArcGIS. Plotted locations are sample sites. Stream flow is northeast.

Clear Creek is a small tributary for Ioway Creek in Ames, Iowa, and part of the Des Moines lobe of the Wisconsinan-aged glaciation. Clear Creek has intermittent iron mineralization forming predominantly within stagnant pools. Four areas with intermittent but recurring iron

mineralization were identified within a 0.20-mile reach of the stream running through the Iowa State University campus. The upstream site is Bridge Top (BT) (42° 01' 54.90012"" N,093° 39' 16.30008"" W), the two midstream sites are Log Jam (LJ) (42° 01' 56.306658"" N, 093° 39' 11.470572"" W) and Beaver Dam (BD) (42° 01' 56.70012"" N, 093° 39' 11.40012"" W), and the downstream site is Dead End (DE) (42° 01' 58.583388"" N, 093° 39' 11.4695028"" W) (Figure 1). Each site had different iron accumulation patterns that may have been related to in-stream debris and water flow paths. Over the past decade, the creek has experienced a maximum 24-hour precipitation of 4.48 inches, with a mean annual precipitation of 34.39 inches (USGS, 2022).

Piezometers

Two piezometers were installed in April 2024 to characterize the soils near the stream and determine the iron concentrations in groundwater and soil. The first piezometer was installed near the stream at coordinates N 42.03220 and W 093.65303. The second one is within 5 m of the first one, but further from the creek at coordinates N 42.03228 and W 093.65314 (Supplemental Figure 1). A bucket auger was used to drill ~20 cm deep for each section of soil until hitting the water table. Soil sections were aligned sequentially and characterized using the Munsell color chart. Soil samples were collected from alternating sections from the surface to the water table, placed in whirlpack bags, and frozen at -20 ºC until further analysis for iron concentrations.

Observations and Geochemical Measurements

Observations of iron mineralization and geochemical measurement sampling were done in tandem at each site at least weekly when temperatures were above freezing during the study period (October 2021 to December 2023). When frozen, the creek was observed and/or sampled at monthly intervals. During the open water season, observations were made no more often than every three days with at least a three-day gap between observations.

Physicochemical measurements of pools were made using a YSI ProDSS multiparameter probe. The measurements included dissolved oxygen (mg L^{-1}), temperature (ºC), specific conductance (µS cm^{-1}), pH, and ORP. For piezometer data collection the YSI ProDSS was lowered to the water table for data collection. Clear Creek was sampled at the same time as piezometers. When there was visible iron in the sampling pools, the observed iron type (Table 1) was recorded, and the pool volume was estimated based on the dimensions of the two longest axes of each pool and its maximum depth.

Phosphorous Quantification

Total phosphorus (TP) and orthophosphate (OP) were determined in both water table samples from the piezometers and from Clear Creek using a modified TP and OP method from Murphy and Riley (1962). For piezometers, a bailer was used to fill 15 mL conical tubes, and separate 15 mL conical tubes were dipped into pools in Clear Creek. Samples were brought back to the lab and analyzed right away. For OP, water was filtered with a 0.45 µm filter into a new 15 mL conical tube. To determine OP, a fresh phosphorus color reagent was made by adding sulfuric acid solution, potassium antimony tartrate solution, ascorbic acid solution, and molybdate solution. After 30 minutes of dark incubation, samples were analyzed on an Epoch 2 Microplate Reader (Biotek) at 885 nm. TP was determined with a 1.6% solution of potassium persulfate. Tubes were placed in the autoclave for 30 minutes at 121.5 ºC. Tubes were cooled to room temperature before following the same procedure as OP for analysis of TP at 885 nm.

Iron Quantification

Two methods were used to quantify total iron in the water. Unfiltered samples were collected in a 15 mL conical tube. Samples taken immediately back to the lab were prepared for quantification using the Hach TNT 890 Metals Prep Set. Iron concentrations were determined using the TNT 858 method on a Hach DR1900 Portable Spectrophotometer. For the second method, unfiltered water was collected in a 15 ml conical tube and immediately acidified with 6M hydrochloric acid (HCl) to a final concentration of 1M HCl. Ferrous iron [Fe(II)] was determined with the Ferrozine assay following a protocol adapted from Stookey (1970) and Viollier et al. (2000) using an Epoch 2 Microplate Reader (Biotek). Total ferrous iron [Fe(II)] was determined with the Ferrozine assay and then again after hydroxylamine hydrochloride reduction to determine total Fe. Then, Fe(II) was subtracted total Fe to determine Fe(III). Samples were diluted if concentrations exceeded the detection range (10 – 300 μM).

Pool sediments were sampled into 15 mL conical tubes for iron extractions. If not processed immediately, samples were stored in a -80°C freezer. Thawed or newly collected samples were placed in a Captair Pyramid 2200A Multi-function Disposable Glovebox flushed with N_2 gas (Erlab, #17404CN) for Fe extraction to prevent speciation changes in iron due to the presence of oxygen. In the glove bag, half a gram of wet sediment was weighed and placed into stoppered serum bottles. Anoxic sodium acetate solution (25 mL) was added to the bottles and shaken at room temperature for 1 hour to solubilize the sorbed iron from sediments. After centrifugation for 20 minutes at 2300 g, the supernatant was extracted to quantify sorbed iron with Ferrozine as described above. The crystalline ferriferous phase was extracted with 25 mL of anoxic 6M HCl. For this treatment, samples were shaken for 24 hours at room temperature and centrifuged to extract the supernatant. Both extractions were analyzed with the ferrozine assay to quantify iron. Three sub-samples were extracted from each sample for triplicate measurements.

Soils that were frozen after piezometer installation were processed similarly to the pool sediments, with one change to the protocol. One gram of soil was weighed and placed into a serum bottle instead of 0.5 g for better detection of the low-quantity adsorbed fraction.

Microbial community analysis

To investigate the microbial community of pools, 500 mL of water was passed through a series of sequential filters (11 μm nylon and 3 and 0.22 μm PES filters; Millipore) with a Masterflex Portable Peristaltic Sampler (Cole/Parmer). The 11 μm filter captured larger phytoplankton, and this study did not investigate these samples further. The 3 and 0.22 μm were expected to capture particle-associated and planktonic microbial cells, respectively. Filters were stored at -80°C in cryovial tubes with RNase later (Lambrecht et al., 2020). Total community DNA was then extracted from the biomass on the filters using a modified DNeasy Powerbiofilm Kit: the original centrifugation step was omitted as the entire filter was used. Also, 30 μL of elution buffer was used instead of the recommended 100 μL to concentrate the DNA. Prior to sample submission, DNA concentration was quantified by Qubit 2.0 Fluorometer at the Iowa State University DNA sequencing facility. All samples were diluted to a concentration of ~20 ng. The V4 region of the 16S rRNA gene was amplified using the primer pair 515 F (5′-GTGCCAGCMGCCGC GGTAA-3′) and 805R (5′-GACTACVSGGGTATCTAAT-3′) using a dual index approach (Kozich et al., 2013). Samples were sequenced on an (Illumina Miseq) using 2 × 250 bp at the Iowa State University DNA Facility.

Sequences were trimmed and quality screened using DADA2 package in R (Callahan et al., 2016). Forward and reverse sequences were trimmed at 225 and 195 bases, to account for differences in quality plots of reverse and forward reads. Reads were denoised, merged, and screened for chimeric sequences for removal, and actual sequence variants (ASV). The phyloseq package was used to create the taxonomy and sample table for further analysis. The decontam package was used to identify and remove ASVs associated with negative controls (Davis et al., 2018). Negative controls from elution buffer and water were run through the same DNA isolation kit and evaluated using the prevalence method. A threshold value of 0.5 was set and used to create a new phyloseq object. We assigned taxonomy with an updated cyanobacteria inventory, Cyanoseq database, which encompasses the Silva database (CyanoSeq 1.2; Silva 138.1) for better accuracy of this phylum (Lefler et al., 2023). For further analysis, sequencing reads from the 0.22 and 3 μm filters were pooled for each sample. Relative abundance of microbes were rarefied, and all organisms were grouped into an "other" category, while putative iron-reducing and oxidizing ASVs were graphed separately to interpret abundance change in samples. Principal Coordinates Analysis (PCoA) was conducted in phyloseq using the default Bray-Curtis dissimilarity and differences were declared significant based on p-values <0.05. All sequences from the tagged Illumina MiSeq libraries were submitted to the NCBI short-read archive under bioproject number (PRJNA1053376).

Scanning Electron Microscopy and Transmission Electron Microscopy Analysis

Field-Emission Scanning Electron Microscopy (FE-SEM) was used to image iridescent films. The iridescent film was scooped onto a silica oxide wafer. Samples were analyzed both without preventing oxygen and exposure, and by keeping anoxic. In the second case, the sample was transported in a Pyrex container with an AnaeroPack (Fischer Scientific) prior to placing in an anoxic glovebox (100% N_2) to prevent further oxidation before analysis. Images of the iridescent iron film deposited on the wafer were analyzed using a ThermoFisher (FEI) Teneo Lovac microscope at the Ames National Laboratory's Sensitive Instrument Facility. Secondary electron images were taken of the stub on low magnification with no coating and low vacuum mode. Backscatter images were taken at varying accelerating voltages of 1, 3, 15, and 20 kV, and high magnification low voltage was used to image the film 'crust.' Additional images were taken in Optiplan mode, and high vacuum/Standard mode, using a Lo-vac (LVD detector), or an Everhard-Thornley Detector (ETD).

For TEM analysis, an acid-washed petri dish was used to scoop water with iridescent film and placed in a glass Pyrex container with an AnaeroPack (Fischer Scientific), which reacted with any trace oxygen in the container to maintain an anoxic atmosphere during transport, so no further oxidation occurred before analysis. The FEI Titan Themis Cubed Aberration Corrected Scanning Transmission Electron Microscope (STEM) was utilized to acquire TEM images of the films. The sample was placed on a copper grid with a carbon film. Energy dispersive spectroscopy (EDS) was used to determine the elemental composition of the films. The FEI Tecnai G2-F20 scanning transmission electron microscope was utilized for Selected Area Diffraction Pattern (SADP) to obtain diffraction patterns of iridescent films to determine the mineralogy based on available reference data. High-angle Annular Dark Field (HAADF) was paired with Electron energy loss spectroscopy (EELS) to obtain high-contrast images and determine iridescent films iron oxidation state and chemical composition. Reference spectra for the iron oxidation state were made with 2-line ferrihydrite [Fe(III)] (precipitated according to

Schwertmann and Cornell, 2000) and hercynite [predominantly Fe(II), but our sample likely contained some Fe(III)].

Results & Discussion

Iron Mineralization

Observations across a year-long sampling period led to the categorization of three main iron mineralization types within four sites of Clear Creek (Table 1).

Table 1: Iron mineralization types. Scale bars are in centimeters.

Mineralization Type	Description	Image of iron mineralization type
Flocculent Iron Mats	Soft, fluffy orange-brown mat attached to sediment surfaces that has the appearance of wet peanut butter. Found in areas of low or no flow.	
Iridescent Films ("schwimmeisen")	Floating, iridescent and/or metallic surface films that resemble oil but break up upon disturbance, unlike oil. Found only in stagnant pools.	
Solid mineral precipitates	Bright orange minerals staining the sediment surface of stagnant pools.	

Flocculent iron mats were found in the midstream sites (LJ and BD). Multiple studies have found flocculent mats in different aquatic habitats ranging from neutral groundwater seeps,

sea mounts, deep hydrothermal vents, or roadside ditches (Emerson & Revsbech, 1994; Rentz et al., 2007; Roden et al., 2012). Flocculent iron mats that house FeOB play a significant role in the biogeochemistry of the environments in which they occur through the degradation of organic compounds and pesticides, and the removal of heavy metals and phosphorous (Fabisch et al., 2013; Rentz et al., 2009).

Iridescent surface film found only at stagnant pools in the midstream sites. In the literature, these films have been called 'schwimmeisen', German for 'floating iron' (Grathoff et al., 2007). However, multiple studies have also observed an iron 'sheen' that sits on top of stagnant water (Almaraz et al., 2017; Perkins et al., 2016; Sánchez-España et al., 2023). Moreover, it has been observed that rainfall and wind will disturb these films (Grathoff et al., 2007).

Lastly, rust-colored solid mineral precipitates were found in some sample sites.

Table 2: Persistent pool locations and features. Characterizations of iron persistence will be identified based on Table 1. Includes size of the pool, stagnant or flowing water, or iron types. Areal extent of iron was based on average measurements of the pool area with measuring tapes as seen in Table 1.

Pool Name	Location	Water Flow	Iron Types	Areal extent of visible iron
Bridge Top (BT) Upstream	42° 01' 54.90012"" N, 093° 39' 16.30008"" W	Medium flow into a stagnant side pool	Little mineralization	Small area 10 in^2 – 20 in^2
Log Jam (LJ) Midstream	42° 01' 56.306658"" N, 093° 39' 11.470572"" W	Stagnant to low flow during rain events, stagnant pools after rain	Iridescent films and precipitates	Large area 24 in^2 – 36 in^2
Beaver Dam (BD) Midstream	42° 01' 56.70012"" N, 093° 39' 11.40012"" W	Low flow on the dammed side; Medium flow on upstream side	Iridescent, flocculent, and precipitates (medium flow)	Large area 36 in^2 – 48 in^2
Dead End (DE) Downstream	42° 01' 58.583388"" N, 093° 39' 11.4695028"" W	High flow with a meander	Little mineralization (only 2 days of visible iron)	N/A

Temporal In-Stream Hydrological and Geochemical Conditions

Clear Creek was repeatedly sampled at four unique locations for water chemistry, iron concentrations, and speciation in water and sediments, and observations of the three iron mineralization types throughout a single year across three seasons. Locations of sampling sites are found in (Figure 1), while the pool characterization data is found in (Table 2).

Site BT (Figure 1), furthest upstream, was near the start of the deciduous forest zone of our sampling area. The site had small accumulations of organic debris near the stream's edge where the water was not obstructed. Consistent flows were observed throughout sampling, although only a small pool remained during prolonged dry periods. Dissolved oxygen (DO) was consistently above 7 mg L^{-1}, but this site had the lowest specific conductivity of all sites throughout the sampling period, ~400 µS cm^{-1} (Figure 2).

The midstream sites LJ and BD (Figure 1) were impacted by wood and organic debris that created small dams, effectively slowing the water flow through these two stretches and

creating pools. The midstream sites had the lowest DO concentrations during October 2021, < 2 mg L^{-1} (hypoxic). Specific conductance was also consistently >500 µS cm^{-1} at these sites during all sampling periods (Figure 2). Increased specific conductance from the upstream site (BT) to the midstream sites (LJ and BD) indicates input of an additional water source with higher dissolved solutes. There are no surface inlets along any of the four sites (Figure 1).

Downstream site DE (Figure 1) had similar specific conductivity measurements as the midstream sites >500 µS cm^{-1} (Figure 2). However, the DO concentrations were consistently above ~4 mg L^{-1} (Figure 2). Like the upstream site, little debris obstructed the water flow. The higher specific conductance at site DE compared to the upstream site BT was likely due to sourcing water from the pools developed in sites LJ and BD.

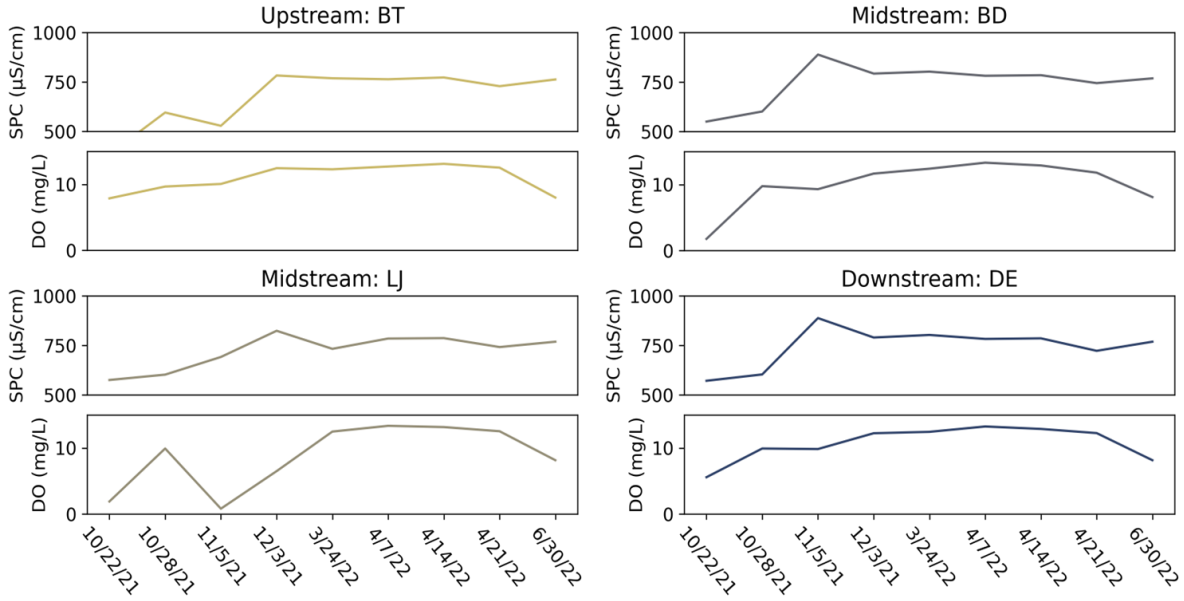

Figure 2: Each site listed in Table 2 was measured once at each sampling time for specific conductivity (SPC) and dissolved oxygen (DO).

Precipitation data were retrieved from the Ames Municipal Airport (KAMW) in Ames, Iowa, and the Automated Surface Observing System (ASOS) data was downloaded from Iowa State University's Mesonet (https://mesonet.agron.iastate.edu/request/download.phtml). Publicly available rainfall records over three seasons, from October 2021 to July 2023, are presented in Figure 3. Regular monitoring observations during the open water season indicate that iron mineralization occurred in the stream days after rain events, but not when the creek was dry. At the end of 2021, several precipitation events were followed by visible mineralization (dashed lines in Figure 3). Little precipitation fell from January until March 2022, and the stream was frozen. Precipitation and snowmelt enhanced observed creek flows and iron mineralization was observed in the weeks after. Very little rain fell from late May to early June 2022, leading to a dry creek bed and no iron mineralization. Mineralization was observed again after several multi-inch rainfall events in December 2022. However, mineralization was not observed following a 9-inch rainfall event in late June 2022. This is likely due to high flows preventing standing pools of

water, as mineralization was typically observed in standing pools, and /or high flows washing away mineralization.

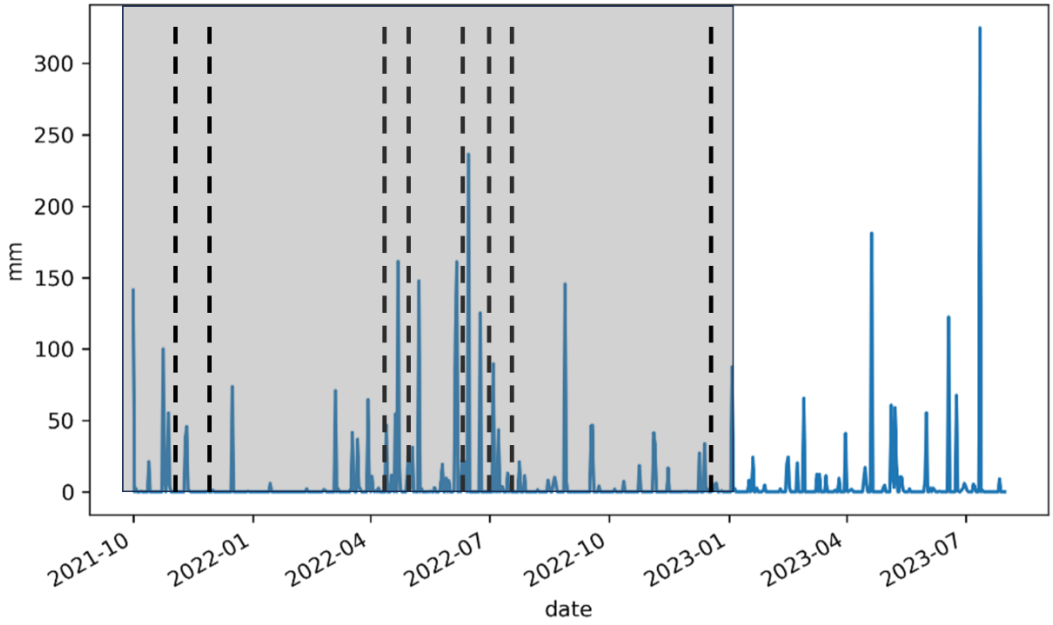

Figure 3: Average precipitation based on weather data collected from the local system. Dashed lines indicate times when iron mineralization types were visible. A grey box indicates the time frame for observations of iron visualizations with geochemical data presented in Figure 2 and Table 3.

Processes for enhancing iron concentrations in mineralized pools

We wanted to understand if iron in the pools was mobilized from rain and direct runoff or added from sediments or groundwater. Enhanced iron contents and mineralization in the creek could result from runoff transporting iron from the watershed into the creek and pools. Previous work on the Corbeira catchment in NW Spain found that higher rainfall years led to increased Fe loads in the stream compared to lower rainfall events coinciding with lower Fe loads (Soto-Varela et al., 2015). Increased precipitation can correlate with elevated dissolved iron levels, along with varied colloidal iron, compared to dry events (Rosenberg & Schroth, 2017; Zhang et al., 2020). If this were the case, we would predict similar total iron concentrations in water from the pools with and without visible iron mineralization (Figure 4). There was no statistical difference in total iron concentrations from water in pools with visible iron mineralization than those without (Figure 4), indicating that the water in the pool is unlikely to supply iron for mineralization. Consistently oxic conditions in the upstream and downstream sites with flowing water indicate that any dissolved Fe(II) would be oxidized to Fe(III) and rapidly precipitated in circumneutral waters, resulting in minimal in-creek transport. Our methods did not specifically assess the presence of complexed or colloidal iron that could be transported simultaneously with the dissolved load of the creek.

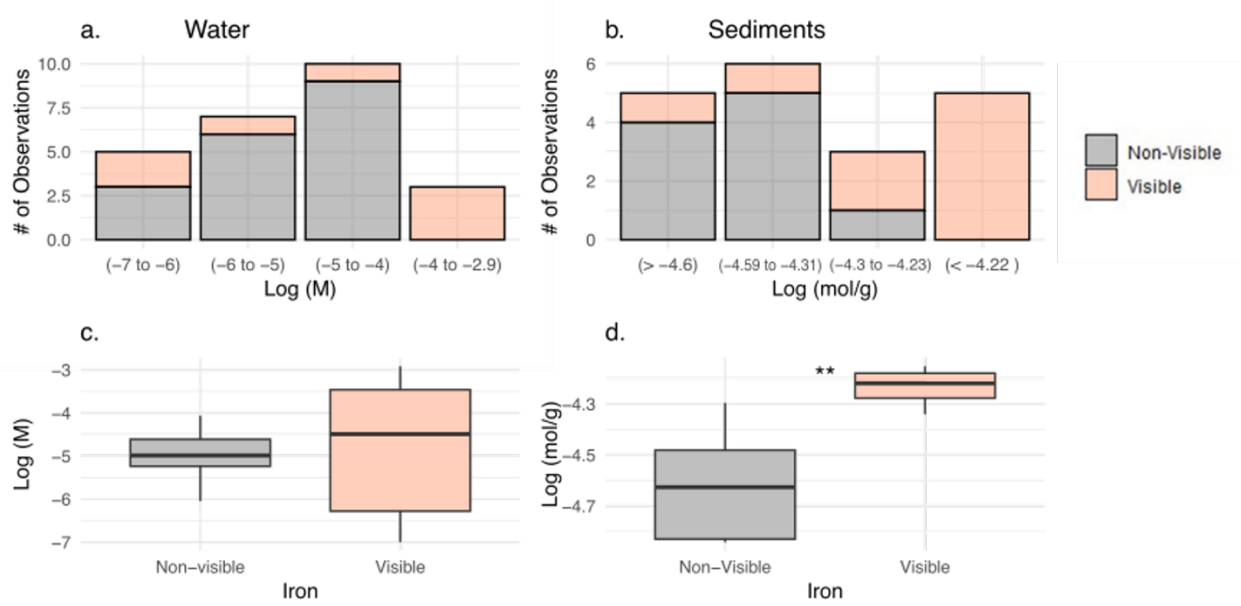

Figure 4: Histogram comparing visible and non-visible mineralization of iron frequency and range of total iron concentrations in a) water or b) sediments. Box and whisker plot depicting ranges of iron concentrations in c) water or d) sediments. Stars indicate statistically significant values (** = < 0.01).

However, there was a significant increase in the amount of iron within sediments of pools with visible iron mineralization compared to those without. The higher iron content in mineralized sediments indicates that iron must be added to the mineralized pools from another source besides pool or creek water (Figure 4). A process that adds iron to the creek sediments is required to explain the observation that visibly mineralized pools have higher sedimentary iron contents but not higher water iron contents. A plausible mechanism from the discharge of anoxic groundwater bearing dissolved Fe(II) from the surrounding soils/sediments, and/or hyporheic circulation of creek water, picking up dissolved Fe(II) as seen from the soil and groundwater Fe concentrations (Table 3). Groundwater inputs and/or enhanced hyporheic exchange would increase dissolved ions relative to water from precipitation and inputs could account for the higher specific conductance values (Figure 2) in the midstream sites (LJ, BD) relative to the upstream site (BT). The lowest DO values in midstream sites (LJ and BD) also correspond to times when mineralization occurred and are consistent with either discharge of anoxic groundwater or development of reducing conditions that could draw down in pool dissolved oxygen. Notably, the mean percentage of baseflow to annual stream flow in Clear Creek is 53.98%, underscoring the substantial contribution of groundwater discharge to the water budget of the system (USGS, 2022).

Clear Creek receives water from precipitation amended with groundwater discharge and runoff from surrounding sediments and deciduous vegetation. Research in northeastern Belgium at the Kleine Nete catchment found that increased base flow introduces enriched Fe(II) groundwater, which is oxidized and precipitated on the stream bed (Baken et al., 2015). Another site with iron mineralization - West Berry Creek in Santa Cruz, California, U.S.A., has average regional precipitation less than ~1 inch and also likely receives iron inputs from groundwater (Duckworth et al., 2009). The damming effect at sites LJ and BD in Clear Creek could have created a longer hydraulic residence time of stream water, enhancing hyporheic exchange or

shallow groundwater recharge/discharge. Similarly, beaver dams sites in Coal Creek and East River, Colorado, U.S.A. had higher specific conductivity in groundwater compared to the stream, with recharge flows transporting dissolved Fe(II) to stream beds (Briggs et al., 2019).

Shallow groundwater could provide a source of dissolved Fe(II) due to microbial reductive dissolution of Fe(III) (oxyhydr)oxides with organic carbon within the floodplain sediments. These floodplain sediments adjacent to Clear Creek are materials such as silt and clay that can naturally accumulate leaf litter and wood debris over time. Water infiltrates the floodplain during high rainfall, and ensuing anoxia allow microbial Fe(III) reduction with clay materials and organics due to the high surface area and saturated environment to enhance Fe(II) mobilization (Table 3). Rainwater mobilizes this Fe(II), allowing a recharge to the groundwater due to the porosity of the deeper floodplain sediments composed of massive pebbly sand, and massive gravelly sand (Table 3). Soils surrounding Clear Creek are > 98% soil Type B from the Soil Survey Geographic Database (SSURGO), composed of sandy soils, an above-average infiltration, and less aggregated loess (Table 3; USGS, 2022). The rising water table establishes the hydraulic gradient, causing Fe-rich groundwater to flow into the creek.

The sediments retrieved during piezometer installation had noticeable iron mineralization at the water table. The piezometers were placed within 5-8 m of the creek, upgradient due to high ground on an adjacent hillslope. In September 2024, the water table elevation measurements in both wells indicated shallow groundwater flow toward the stream with a hydraulic gradient of 0.07245 m m^{-1}. Our data indicates a plausible mechanism for the introduction of Fe(II) into the creek through shallow groundwater discharge that is elevated in the days following precipitation events, noticeable as iron mineralization, but after the runoff through the creek has subsided enough so mineralization is not washed away.

Table 3: Representative sediment characteristics ascertained during piezometer installation, and resulting groundwater geochemistry within the piezometer (blue shading) Abbreviations: Dissolved Oxygen (DO), Oxidation-Reduction Potential (ORP), Specific Conductance (SPC), Orthophosphate (OP), and Total Phosphorous (TP) are represented within the table. Averages of Clear Creek geochemical data compared to the same time point of piezometer sampling appear as a sidebar.

Piezometer Well #1, nearest to Clear Creek				
Depth (m)	Soluble Fe fraction (log mol/g)	Total Fe mineral fraction (log mol/g)	Soil Type *Subangular blocky (SBK)	Munsell color scale
0 – 0.20	-5.66	-4.17	Granular silty clay	10YR2/2
0.20 – 0.41			SBK silty clay	10YR2/2
0.41 – 0.61	-4.83	-4.09	SBK silty clay	10YR2/2
0.61 – 0.81			SBK silty clay	10YR2/2
0.81 – 1.02	-5.48	-3.82	SBK silty clay	10YR2/2
1.02 – 1.22			mottled, SBK sandy clay	10YR2/2
1.22 – 1.42	-5.12	-3.66	mottled, SBK sandy clay	10YR2/2
1.42 – 1.63			mottled, SBK sandy clay	10YR2/2
1.63 – 1.83	-5.46	-4.39	Massive loam	5Y2.5/1
1.83 – 2.03			Massive sand	2.5Y3/2
2.03 – 2.24	-5.84	-5.04	Massive sand	2.5Y3/2
2.24 – 2.44			Massive pebbly sand	7.5YR3/4
2.44 – 2.64	-5.21	-4.18	Massive pebbly sand	7.5YR3/4
2.64 – 2.85			Massive gravelly sand	7.5YR3/2
2.85 – 3.05	-5.31	-3.99	Massive gravelly sand	7.5YR3/2
Water Table Total depth below surface = 3.35 m Depth to water table = 1.42 m	OP = 20.83 ± 1.07 µg L^{-1} TP = 57.27 ± 1.39 µg L^{-1} OP/TP ratio = 0.36 ± 0.01	pH = 6.92 ± 0.07 ORP = 181.2 ± 33.34 mV	SPC = 922 ± 30.74 µS cm^{-1} Total Fe = 46.64 ± 12.95 µM	DO = 1.02 ± 0.17 mg L^{-1} Temperature = 13 ± 0.17 °C

Clear Creek Average Geochemical Conditions
pH 8.01 ± 0.36 ORP 181.53 ± 12.72 mV
SPC 762.14 ± 38.82 µS cm^{-1} DO 11.96 ± 0.87 mg L^{-1}
Temp 13.1 ± 0.83 °C
OP 65.05 ± 3.14 µg L^{-1} TP 116.51 ± 13.91 µg L^{-1}
OP/TP ratio 0.61 ± 0.075

Soil samples from piezometer installation were used to determine the iron fractions in each soil type to test for Fe availability (Table 3). Loosely adsorbed iron fractions ranged from -5.84 to -4.83 log mol/g, with the highest concentration found in the depth interval of 0.41 – 0.61 m below the ground surface (Table 3). The total Fe mineral fraction exhibited higher concentrations, ranging from -5.04 to -3.66 log mol/g (Table 3). These numbers are consistent with previous literature on sandy soils from Iowa, where free iron in whole soils was between -4.90 to -4.10 log mol/g (Folks and Riecken, 1956). Moreover, a report by (Leopold, 2010) indicated on average deep Iowa soils contained -3.32 log mol/g Fe and -3.38 log mol/g Fe in shallow soils.

The wells were screened over the entire interval to capture the water table. The water was analyzed for various geochemical parameters to identify differences between the in-stream

profiling. Orthophosphate (OP) averaged 20.83 μg L^{-1}, and total phosphorus (TP) averaged 57.27 μg L^{-1} (Table 3). These findings align with a larger-scale study of different streams and river systems around Iowa, which report OP concentrations ranging from 40 – 210 μg L^{-1} OP and TP concentrations between 280 – 550 μg L^{-1} TP (Schilling et al., 2017). Notably, Clear Creek had on average higher OP/TP ratios than groundwater, suggesting an external source of P loading to the system. This could be indicative of soil erosion, runoff, or due to the watershed being predominantly agricultural (Fox et al., 2016; Gentry et al., 2007). However, some geochemical parameters differed between in-stream and groundwater measurements. For instance, dissolved oxygen in piezometers was consistently lower on average (1.02 ± 0.17 mg L^{-1}) than the in-creek sampling sites (11.96 ± 0.87 mg L^{-1}), and the pH was (6.92 ± 0.07) compared to (8.01 ± 0.36) in the creek (Table 3). These parameters indicate a reducing environment, which could supply Fe(II) to the stream.

Putative Fe-cycling Microbial Community

Our data support the hypothesis that recent rainfall drives enhanced groundwater discharge and/or hyporheic exchange, particularly through dammed sections of the stream, bringing in a source of dissolved Fe(II) to the pools from the surrounding soils and sediments that result in visible mineralization. Discharge of Fe(II) can promote the development of in-pool iron mineralization by microbes such as FeOB. Inputs of organic carbon such as are supplied from in-creek wood, could support heterotrophic microbes and FeRB. This has been documented in streams with organic debris or beaver dams, which divert water through sediments and result in iron staining (Briggs et al., 2019; Lautz et al., 2006). Both Fe(II) and Fe(III) in Clear Creek's sediments suggest active redox cycling of iron.

We therefore assessed whether putative Fe(II) oxidizing and/or Fe(III) reducing microbes were more prevalent in mineralized vs. non-mineralized pools. Moreover, previous work on regenerative stream water conveyance structures found flocculant mat formations forming near site structures where groundwater carries Fe(II) leaching from constructed material promoting FeOB growth (Williams et al., 2016). Iron seeps located in Prince William County, Virginia, U.S.A. discharged anoxic, Fe(II) rich groundwater to the microbial community, aiding in co-occurring iron mineralization and microbial mats (Rentz et al., 2007).

16S rRNA sequencing was performed on 22 water samples from pools with visible and 17 water samples from pools with no visible mineralization. The samples from pools that contained visible iron mineralization were further demarcated based on the mineralization type present during sampling: I: iridescent (5), P: precipitates (12), I, P: both iridescence and precipitates (2), and PIF: all three iron types but dominated by flocculant iron mats (3). Further analysis determined grouping differences through microbial richness, evenness, and relative abundance. Four samples were removed from further analysis due to inadequate initial library sizes <40,000, due to control samples containing an equal or greater number of sequences. A total of ~200 contaminant taxa were removed from the remaining samples after decontamination.

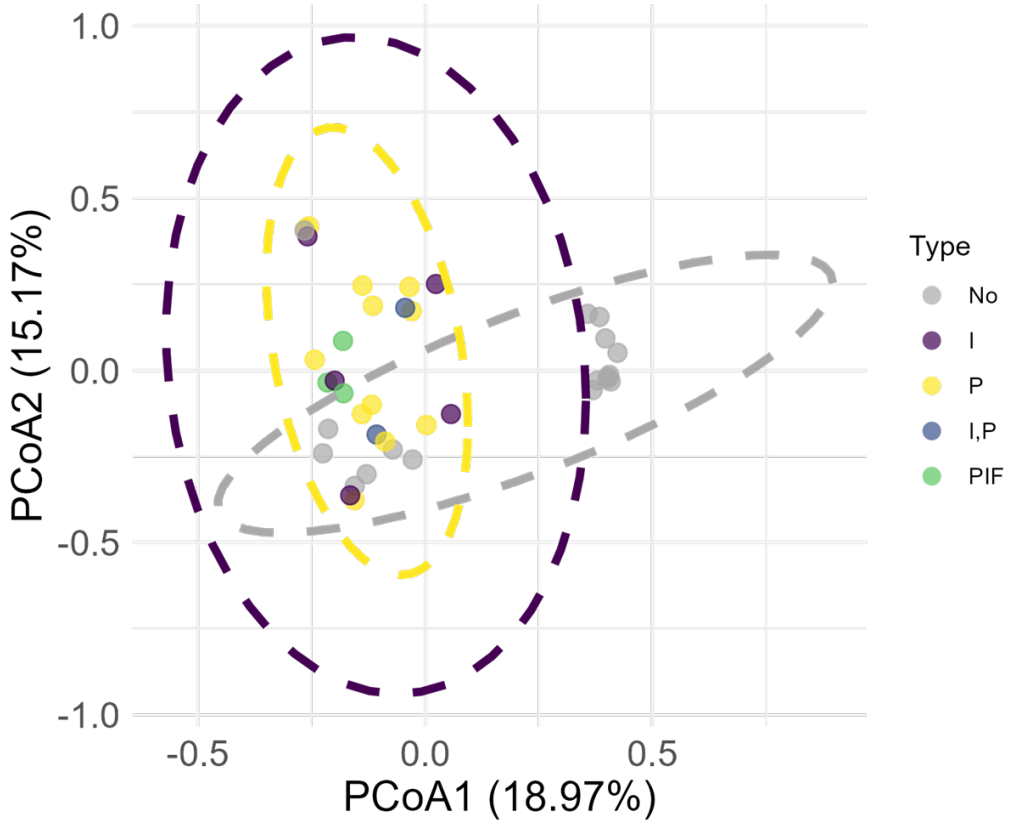

Figure 5: Principal Coordinates Analyses (PCoA) conducted based on Bray-Curtis dissimilarity highlighted the distinct communities of visibly mineralized samples, which clustered on the left side of the plot, and no visible mineralization samples, which clustered on the right side of the plot but also included some samples that clustered with visibly mineralized samples. Ellipses are plotted with a 95% confidence interval and plotted with the percentage of variability on the axis. Variables I,P and PIF did not have enough data points to calculate the ellipse for those samples. Legend labels: No: no visible iron, I: iridescent, P: iron precipitates, I,P: both iridescence and precipitates, and PIF: all three iron types. Permanova analysis revealed a p-value = 0.001.

The Shannon, Simpson, and Chao1 indexes determined the alpha diversity of visibly mineralized and non-mineralized samples (Supplemental Figure 2). Principle Coordinates Analysis (PCoA) using the Bray-Curtis dissimilarity data between iron types revealed two major clusters (Figure 5). The first (left) cluster was comprised mostly of all visibly mineralized samples, with some non-mineralized samples. A second (right) cluster contained exclusively not visibly mineralized samples (Figure 5). Based on a Permanova analysis, there was a significant difference (<0.05) between the left and right clusters (Figure 5). This clustering was not related to site location (Supplemental Figure 3). However, a significant difference was observed by the season of observation (<0.05; Supplemental Figure 4). Only samples collected in winter non-mineralized samples were in the right cluster, although some winter non-mineralized samples did occur in the first cluster (Supplemental Figure 4). This analysis indicates that mineralization and season were possible drivers of microbial community composition, which is explored further below.

The dominant bacterial phyla detected were Bacteroidota, Proteobacteria, and Actinobacteriota, respectively (Supplemental Figure 5). The pools with iridescent films and flocculent iron had higher abundances of Proteobacteria (45-70%) than the non-visible iron and

492 solely iridescent film samples (Supplemental Figure 5). Our results are consistent with the
493 previous report on iron films in circumneutral wetlands, which indicated Proteobacteria were the
494 highest abundant taxa (~80%) compared to other taxonomic groups (Dong et al., 2024).
495 Proteobacteria relative abundance in porewater and sediments in Mineral and Cement Creeks
496 was between 22 – 78% (Hoagland et al., 2024). Moreover, previous reports support that
497 Proteobacteria are associated with iron cycling and contribute to different iron mineralization
498 (Melton et al., 2014; Kappler et al., 2021), and could be important in various elemental cycling
499 in Clear Creek. Samples clustered on the left in the PCoA (Figure 5) had a higher abundance of
500 Proteobacteria than sample clusters on the right (Supplemental Figures 6 & 7). These findings
501 indicate that visibly mineralized samples may encompass distinct habitats and communities
502 compared to the non-mineralized samples.
503 To further investigate this, we assessed the relative abundance of 16S rRNA sequences
504 typically assigned as iron-cycling bacteria in the different visible iron types compared to non-
505 visible iron samples (Figure 6). Putative FeOB included the families *Gallionellaceae*,
506 *Comamonadaceae*, and *Bacillaceae*, and known FeRB included the families *Geobacteraceae*,
507 *Aeromonadaceae*, *Desulfovibrionaceae*, and *Shewanellaceae*,
508 and *Rhodobacteraceae,* respectively (Figure 6). Not all organisms within these families are
509 putative FeOB. We also included a family of methane oxidizers (*Methylomonadaceae*) because
510 of their potential role in iron film formation (Dong et al., 2024). Moreover, in anoxic waters,
511 these methane oxidizers have a syntrophic relationship with FeRB (Cabrol et al., 2020). Known
512 iron-cycling bacteria do not make up the majority of the microbial community. Specifically, the
513 relative abundance of FeRB found in freshwater lake sediments contained between 3 and 7%,
514 with the highest contributions from *Geobacter* and *Desulfuromonas*, respectively (Fan et al.,
515 2018). One study found in acid rock drainage that the relative abundance of *Gallionella* was (1.5
516 - 4.8%) in sediments from Mineral Creek (Hoagland et al., 2024), compared to our results from
517 water samples, found *Gallionellaceae* to be between 0.5 – 9% in visible iron types. Within the
518 iron films Dong et al. studied (2024), *Geobacter* composed 6.8% and *Gallionella* 6.9% of the
519 microbial community. Our visible iron types are consistent with the previous studies, with the
520 relative abundance of iron-cycling organisms increasing by 3 – 17% overall compared to non-
521 visible iron samples (Figure 6).

522

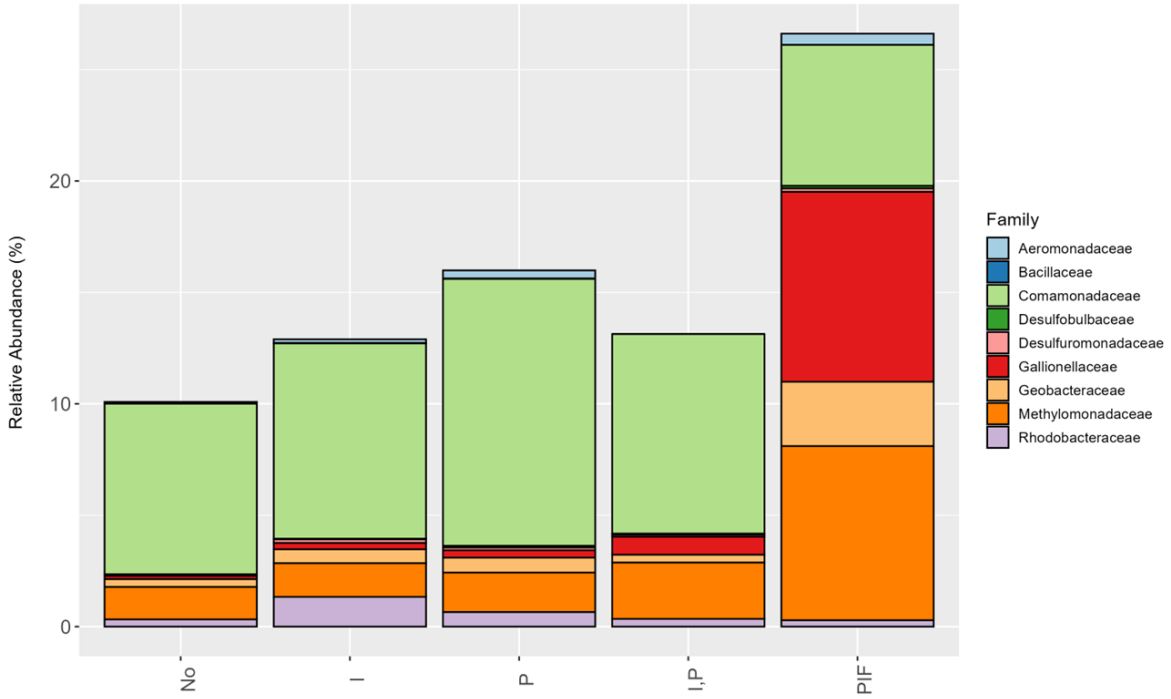

Figure 6: Relative abundance at the Family level of putative iron cycling bacteria + methane-oxidizing bacteria in the different iron mineralization types. Legend labels: No: no visible iron, I: iridescent, P: iron precipitates, I,P: both iridescence and precipitates and PIF: all three iron types.

Gallionellaceae or *Comamonadaceae* were the two most abundant putative FeOB in all samples. *Comamonadaceae* has the highest abundance in mineralized samples but were similarly abundant to *Gallionellaceae* when flocculent mats are present (Figure 6). Previous studies found mineralized iron with a high abundance in both gene copies and relative abundance of *Gallionellaceae* and *Comamonadaceae* in multiple freshwater systems (Blöthe and Roden, 2009; Dong et al., 2024; Fabisch et al., 2013), and these bacteria have been associated with the prevalence of flocculent iron in these different aquatic systems (Brooks and Field, 2020; Williams et al., 2016). The *Methylomonadaceae* relative abundance was elevated in PIF samples compared to all other samples (Figure 6).

Seasonality also affected community composition, with summer having the highest relative abundance of *Comamonadaceae* and *Methylomonadaceae,* while *Gallionellaceae* had its highest abundance in the winter (Supplemental Figure 8). Previous work in Belgium on streams to the Demer River reflected that biological oxidation could outpace the abiotic iron oxidation in the winter months, leading to increased FeOB bacteria (Baken et al., 2015). Another study found similar results with *Gallionella* sp. growth observed under fully oxic conditions, and neutral pH and speculated that biological iron oxidation could outpace chemical iron oxidation at moderate or low temperatures ~13°C (de Vet et al., 2011). Four areas of Graubünden canton in the Swiss Alps with 8 – 12 °C temperatures and a pH <7.4 supported microbial iron oxidation (St Clair et al., 2019). The differences in community composition in non-mineralized samples were also strongly affected by seasonality (Supplementary Figure 4).

Increased abundance of *Geobacteraceae*, and *Rhodobacteraceae* in mineralized samples compared to non-mineralized supports the potential for FeRB growth following the development of hypoxic conditions in Clear Creek (Kappler et al., 2021). These organisms reduce mineralized

Fe(III) coupled to organic matter mineralization, which provides energy to support bioremediation of contaminants (Tobler et al., 2007; Wu et al., 2010). Studies have noted ferrihydrite or schwertmannite can drive microbial Fe(III) reduction (Sánchez-España et al., 2023). Such poorly crystalline Fe(III)(oxyhydr)oxides formed from biotic iron oxidation are good substrates for FeRB coupled to organic matter oxidation. However, despite efforts to quantify poorly crystalline Fe(III)(oxyhydr)oxides in sediment iron extractions, we consistently obtained results below detection limits. The presence of FeOB and FeRB within these mineralized pools could indicate rapid microbial iron oxidation and reduction at the interface of the iron precipitates, flocculent mats, and under iron films. The increased abundance of *Geobacteraceae* with *Gallionellaceae* and *Comamonadaceae* indicates the potential for this dynamic. The sites with the most damming effects contained higher abundances of iron cycling bacteria (LJ and BD) (Supplemental Figure 9), indicating the potential importance of stagnation, lowered DO, and in-creek organic debris to fuel this process. Moreover, phosphorus adsorbed onto Fe(III) (oxyhydr)oxides can be released during Fe(III) reduction, which could additionally promote microbial growth within the pools (Neidhardt et al., 2018).

Although the microbial community associated with iridescent films was not directly sequenced, the results from I and PIF sample types can be informative of taxa that may be associated with iron film mineralization. Previous work has detected the families *Geobacteraceae, Rhodocyclaceae, Gallionellaceae,* and *Methylomonaceae* (Dong et al., 2024). The presence of similar clades within our pools with films may support the idea that both FeOB and FeRB are involved in film formation. The enhanced presence of *Rhodobacteraceae* in iridescent films in our study indicates this organism may also be important to consider for a role in this process in follow-up studies.

Iridescent Iron Film Characterization by SEM and TEM

While many other studies describe flocculent iron mineralization, mineralogy, and microbial processes, fewer studies describe the iridescent iron films' occurrence, characteristics, and possible formation pathways (Almaraz et al., 2017; Dong et al., 2024; Grathoff et al., 2007; Sánchez-España et al., 2023). Based on our collective anecdotal experience, we suspect iridescent films may be a common mineralization type in Clear Creek that is typically not recognized as such because of its similar appearance to organic/oil contamination. Therefore, we followed up with additional analysis to demonstrate that the iridescent film was 1) composed of iron, 2) determine the iron oxidation state, and 3) ascertain the mineralogy

All films displayed similar characteristics when observed under both SEM and TEM. Natural film samples display cracking under SEM (Figure 7a-c), likely due to disturbance and drying during collection. Furthermore, visible rods on the films in SEM images are consistent with colonization by bacteria (Figure 7b). At 20,000X magnification, the films appear smooth on one side and have a rough surface on the other (Figure 7c), though it was not determined which side was in contact with air vs. water in the creek. The films had a maximum thickness of 150 nm, determined in TEM (Figure 8a-b). The iridescent films were similar in chemical composition to previous work (Dong et al., 2024), containing ~70 – 85 atom % oxygen and ~15 – 30 atom % Fe as analyzed by EELS (Figure 8c-d). Most films comprised these two elements; additional elements were carbon and calcium. Carbon was also present as a coating on the copper grid, making quantitative analysis of carbon exclusively from the sample impossible. A composition of 70 atom % oxygen and 30 atom % iron is consistent with Fe in 6-fold coordination with oxygen.

The oxidation state of iron in the iridescent films was assessed with EELS using the reference minerals ferrihydrite for Fe(III) and hercynite for Fe(II). The main energy loss peak based on five different analyses of the iridescent film samples is at 710 eV (Figure 9a-b & Supplemental Figure 10), the same energy as our ferrihydrite standard. Multiple analyses of our hercynite standard indicate it contains both Fe(II) and Fe(III)(Figure 9a). Prior studies of films found mixed valent iron or Fe(III). In the studies of Dong et al., (2024) & Grathoff et al., (2007), TEM grids were allowed to air dry, which could oxidize Fe(II). Our grids were carefully protected from oxygen until analysis, and indicate that Fe(III) can indeed be an *in situ* component of these films.

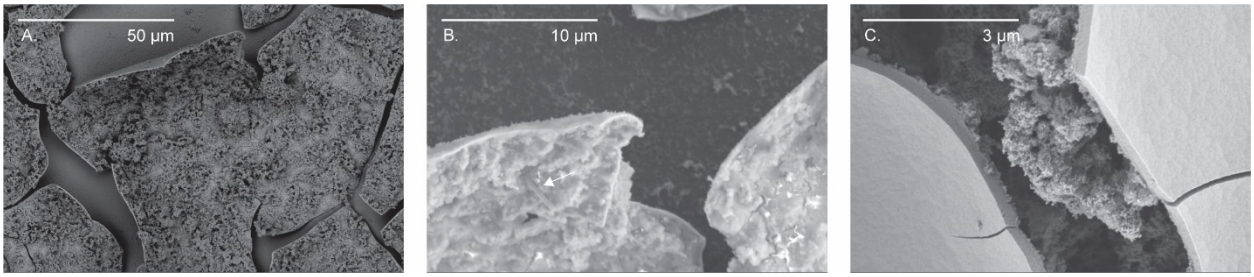

Figure 7 a-c: SEM images of iridescent surface films ("Schwimmeisen") from Table 1. a-c) Magnification increases through the sequence. –b-c) Minerals and/or biomass are attached to the film. White arrow indicates a microbial rod attached to the film.

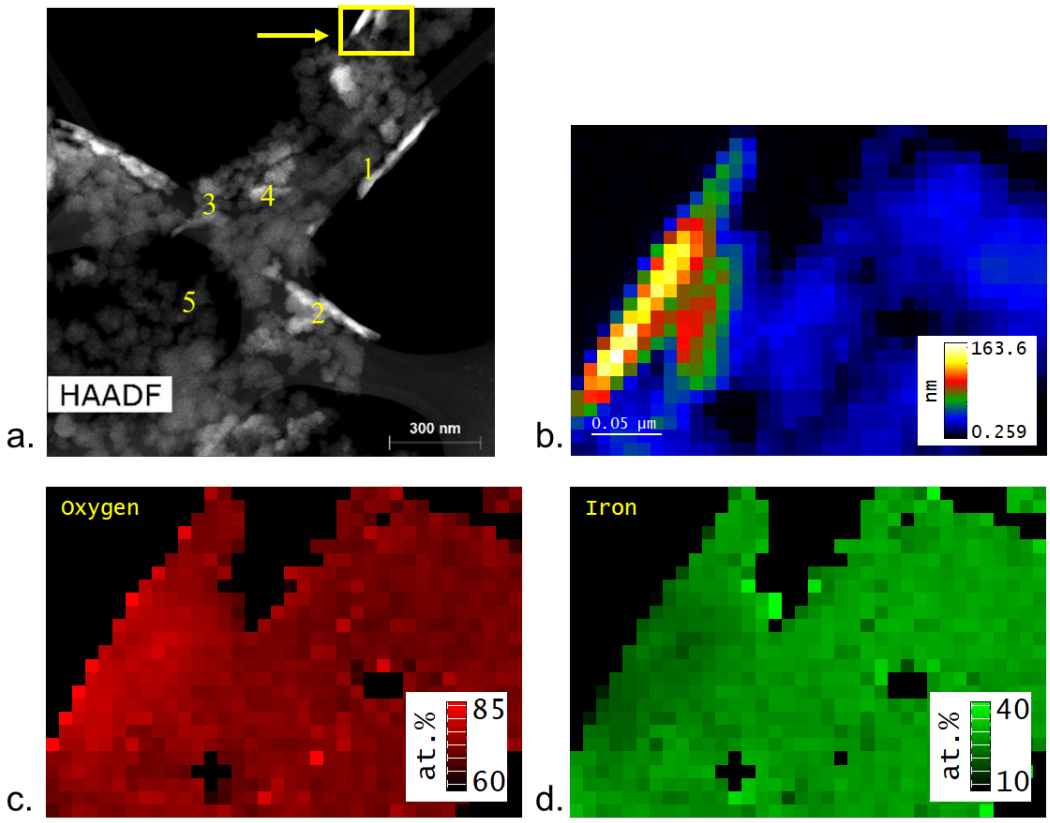

Figure 8 a-d: TEM images of iridescent surface films ("Schwimmeisen") from Table 1. a) HAADF image showing yellow inset analyzed in b-d, and the five areas of interest analyzed by EELS in Figure 9. b) EELS analysis to determine thickness of the film. c-d) Percent composition of oxygen and iron.

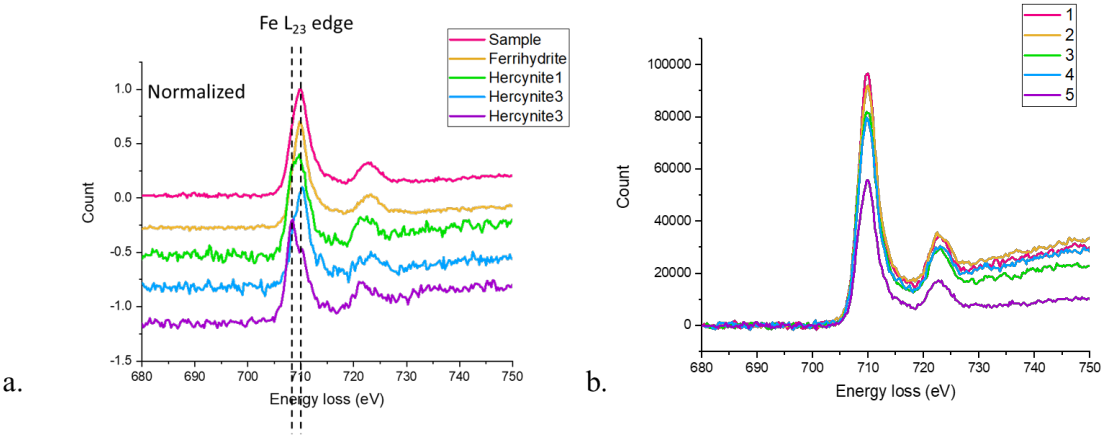

Figure 9 a - b: EELS spectra from iron film in Figure 5. a) Reference samples (Ferrihydrite and Hercynite) were used to determine oxidation state from Sample 1 in Figure 8. b) Fe $L_{2,3}$ edge. The legend corresponds to the 5 areas of interest labeled in Figure 8a.

Selected Area Diffraction Pattern (SADP) gave more mineralogical insights into the films. Two samples analyzed had similar diffraction patterns with interplanar spacings at 2.11, 1.24, and 1.04 Å (Figure 10). Neither of these interplanar spacings corresponds to expected spacings for standard ferrihydrite and fougerite, a carbonate-bearing, mixed-valent green rust (Figure 10). An

interplanar distance of 1.226 ± 0.031 nm has previously been reported for a carbonate green rust (Zegeye et al., 2012). Green rust is unstable in oxygen and forms in more reducing conditions (Feder et al., 2018), where a hypoxic zone under the film could create an ideal environment for green rust formation. However, the availability of anions and parent materials such as phyllosilicates can impact the formation and crystallinity structure (Betts et al., 2023; Trolard & Bourrié, 2006). The spacings in the film are offset from 2-line ferrihydrite interplanar spacings at 2.56 and 1.48Å, although a broad ring was visible at 1.06 to 1.14 Å (Janney et al., 2000). In contrast, Grathoff et al., (2007) XRD of films showed broad peaks at 4.5, 2.6, and 1.5 Å, indicative of 2-line ferrihydrite, and was further studied by Perkins et al., (2016), finding interplanar spacings at 2.6, 3.3-3.5, and 4.4 Å that corresponded to more crystalline forms. These findings are similar to previous TEM analyses done on iridescent films from cascade pools in Northwestern Oregon, U.S.A., and the Kongjiang reservoir, where EELS was used to characterize films composed of ferrihydrite or green rust phases with Fe(II) supplied from groundwater or during microbial iron reduction (Dong et al., 2024; Perkins et al., 2016).

The finding that our film samples interplanar spacings are consistent with one or more rings from 2-line ferrihydrite and carbonate-bearing green rust, and lack larger spacings could be consistent with short-range order and mineral growth truncation, and could be due to differences in the degree of edge-sharing within the lattice (Kleja et al., 2012; Schwertmann & Cornell, 2000; Toner et al., 2009). Disruption of crystal growth could potentially be due to the presence of dissolved ions. Environmental factors such as pH and ionic strength can influence the crystallinity of iron oxides. Specifically, silicate, carbonate, and phosphate ions and organic matter can disrupt the growth of ferrihydrite crystals, leading to variations in observed ring spacings (Rutherford, 2005; Schwertmann & Cornell, 2000). Elevated OP and TP concentrations within Clear Creek compared to groundwater could disrupt mineral growth (Table 3). The distinct lattice spacings we observed could also represent the transformation of ferrihydrite to green rust or vice versa or the disruption of crystal growth by (bi)carbonate ions. Previous work found that ferric minerals can interact with dissolved Fe(II) in anoxic environments and generate green rust (Usman et al., 2012). However, these minerals are less stable, which indicates why some samples appear closer to magnetite with higher stability (Cornell & Schwertmann, 1996). Moreover, in deep-sea hydrothermal vents, it has been hypothesized that biofilms associated with Fe lack the standard crystallinity structure seen in ferrihydrite and goethite due to the presence of Fe-complexing ligands produced biologically (Toner et al., 2009).

In previous studies, organic material was observed to be attached to the films and make up a portion of the overall film composition (Kleja et al., 2012; Perkins et al., 2016; Dong et al., 2024). An intriguing characteristic of iron films is that they float despite being mineralized of typically Fe(III) (oxyhydr)oxides that have specific gravity of (3.3 – 4.3 g cm^{-3}). The rough surface seen in (Figure 7d) could indicate the presence of co-precipitated organic matter. Perkins et al. (2016), indicated that humic acids were crucial for natural nanocrystalline film formation, which could create a hydrophobic lipoprotein structure. Sánchez-España et al. (2023) noted that iron films float due to neustonic microorganisms releasing these organic compounds and exudates and acting as nucleation sites for Fe(III) mineralization. One study found the coprecipitation of organic matter affects the mineralogy during iron cycling (Shimizu et al., 2013). Our results of short-range ordering and lack of a defined mineral structure further emphasized the need to investigate the mechanism of film formation and the co-occurring microbial and organic geochemistry. A likely scenario is that Fe(II) introduced into pools can be

(re-)oxidized at the pool surface by biotic and abiotic processes (Colombo et al., 2014), possibly with ligand-based stabilization of Fe(II). The film could form a barrier from the oxygenated surface, creating a mini-anoxic environment underneath a diverse microbial consortium of FeOB and FeRB to co-inhabit, such as those observed from pools with films by 16S rRNA sequencing (Figure 6). Moreover, the film can form a barrier to protect the neustonic bacteria from UV or high oxygen to help promote iron and nutrient cycling as discussed by Sanchez-España et al., (2023).

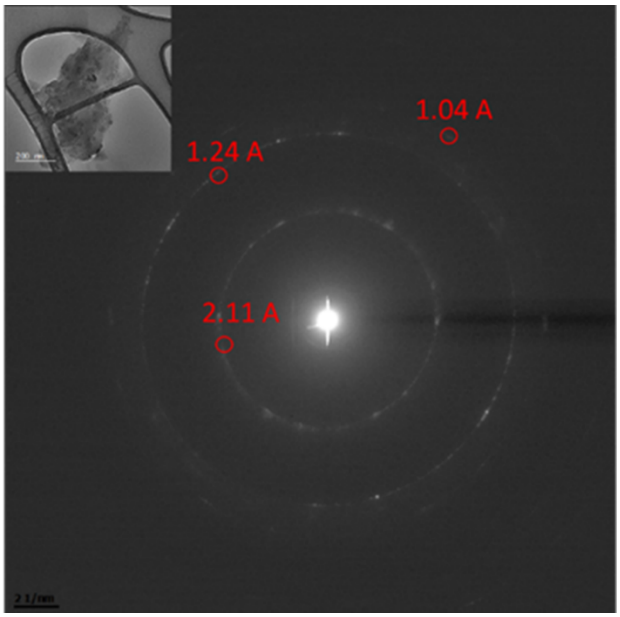

Figure 10: Representative SADP crystallography with interplanar spacings of iridescent sample.

Conclusion

In this study, we report on several types of iron mineralization in an intermittent agricultural stream in Ames, IA, USA. Sediment iron extractions and in-pool iron quantification indicate that the source of iron is not from creek water or creek sediments. Observations that mineralization occurred in pools with elevated specific conductance relative to upstream waters and that mineralization formed in the days following precipitation led us to hypothesize that Fe(II) was added to the creek bed by shallow groundwater discharge. Piezometers placed adjacent to the creek documented that the floodplain sediment contained mobilizable iron, groundwater had low oxygen conditions necessary for Fe mobilization, and a hydraulic gradient existed to drive groundwater discharge into the creek. We further postulate that in-creek organic debris that created small dams and pools, which enhanced hydraulic residence times of creek water recharged through surrounding soils and sediments, which could pick up Fe(II) from floodplain sediments.

The microbial community of pools contained putative FeOB *Gallionellaceae* and *Comomonadaceae* and putative FeRB *Geobacteraceae* and *Rhodobacteraceae*. The abundance of *Gallionellaceae* was elevated in winter, suggesting low temperatures and associated slower kinetics favor biotic over abiotic Fe(II) oxidation. The composition of FeOB and FeRB in pools

with iron films was similar to what has been detected in other studies and indicates taxa to investigate their role in film formation through Fe redox cycling.

Clear Creek had iridescent films floating on the surface of pools that were characterized as short-ranged ordered minerals composed of Fe and O. Their poor crystallinity could be due to the presence of phosphate or (bi)carbonate ions that disrupted mineral growth. These floating films could represent microcosms for iron-cycling microorganisms to thrive by providing essential nutrients (i.e., phosphate, Fe, C, N) or a stable environment with consistent pH or DO.

We believe iron cycling is relevant to agricultural streams due to the reactivity of iron with other microbial processes and the interconnection with phosphorous cycling. Our study provides insight into a potential iron flux to a creek and highlights the importance of coupled physical and biogeochemical processes that result in the observed mineralization. This insight into iron fluxes could be significant for other agricultural streams with intermittent iron and phosphorous inputs from groundwater or runoff, offering a broader understanding of nutrient dynamics in such ecosystems.

Acknowledgments

Thank you to Bienvenido Cortez and Faith Rahem-Seggerman for help with the R analysis. Thank you to Dr. Katy Rico, Michelle Chamberlain, and Dr. Pete Moore for helping review the manuscript before submission. Thank you to Michelle Chamberlain, Dr. Pete Moore, Luis Sosa, John Herring, and Mariela Alfaro-Garcia for helping with piezometer installations. Thank you to Dr. Chris Harding for help utilizing ArcGIS for Clear Creek mapping. Dr. Lisa Mayhew provided the hercynite reference. Thank you to Drs. Jinsu Oh, Lin Zhou, and Matthew Lynn for help on the electron microscopy and related work performed using instruments in the Sensitive Instrument Facility in Ames National Lab. The Ames National Laboratory is operated for the U.S. Department of Energy by Iowa State University under Contract No. DE-AC02-07CH11358. Also, thank you to Oskar Niesen for helping collect the geochemical data.

Funding

This work was funded by the NSF CAREER Award: Quantifying the Extent and Biogeochemical Impact of Modern Ferruginous Lakes (Award 1944946).

References

Ahn, J. S., Ji, S. W., Cho, Y. C., Youm, S. J., & Yim, G. J. (2015). Assessment of the potential occurrence of acid rock drainage through a geochemical stream sediment survey. *Environmental Earth Sciences*, *73*(7), 3375–3386. https://doi.org/10.1007/s12665-014-3625-7

Almaraz, N., Whitaker, A. H., Andrews, M. Y., & Duckworth, O. W. (2017). Assessing Biomineral Formation by Iron-oxidizing Bacteria in a Circumneutral Creek. *Journal of Contemporary Water Research & Education*, *160*(1), 60–71. https://doi.org/10.1111/j.1936-704x.2017.03240.x

Baken, S., Salaets, P., Desmet, N., Seuntjens, P., Vanlierde, E., & Smolders, E. (2015). Oxidation of iron causes removal of phosphorus and arsenic from streamwater in groundwater-fed lowland catchments. *Environmental Science and Technology*, *49*(5), 2886–2894. https://doi.org/10.1021/es505834y

Betts, A. R., Siebecker, M. G., Elzinga, E. J., Luxton, T. P., Scheckel, K. G., & Sparks, D. L. (2023). Influence of clay mineral weathering on green rust formation at iron-reducing conditions.

754 *Geochimica et Cosmochimica Acta*, *350*(May 2022), 46–56.
755 https://doi.org/10.1016/j.gca.2023.04.001
756 Blöthe, M., & Roden, E. E. (2009). Microbial iron redox cycling in a circumneutral-pH groundwater
757 seep. *Applied and Environmental Microbiology*, *75*(2), 468–473.
758 https://doi.org/10.1128/AEM.01817-08
759 Boano, F., Harvey, J. W., Marion, A., Packman, A. I., Revelli, R., Ridolfi, L., & Worman, A. (2014).
760 Hyporheic flow and transport processes: Mechanisms, models, and biogeochemical implications.
761 *Eos, Transactions American Geophysical Union*, *69*(37), 603–679.
762 https://doi.org/10.1029/88EO01108
763 Boulton, A. J., Findlay, S., Marmonier, P., Stanley, E. H., & Maurice Valett, H. (1998). The
764 functional significance of the hyporheic zone in streams and rivers. *Annual Review of Ecology*
765 *and Systematics*, *29*, 59–81. https://doi.org/10.1146/annurev.ecolsys.29.1.59
766 Briggs, M. A., Wang, C., Day-Lewis, F. D., Williams, K. H., Dong, W., & Lane, J. W. (2019). Return
767 flows from beaver ponds enhance floodplain-to-river metals exchange in b mountain catchments.
768 *Science of the Total Environment*, *685*, 357–369. https://doi.org/10.1016/j.scitotenv.2019.05.371
769 Brooks, C. N., & Field, E. K. (2020). Iron flocs and the three domains: Microbial interactions in
770 freshwater iron mats. *MBio*, *11*(6), 1–16. https://doi.org/10.1128/mBio.02720-20
771 Bruun, A. M., Finster, K., Gunnlaugsson, H. P., Nørnberg, P., & Friedrich, M. W. (2010). A
772 comprehensive investigation on iron cycling in a freshwater seep including microscopy,
773 cultivation and molecular community analysis. *Geomicrobiology Journal*, *27*(1), 15–34.
774 https://doi.org/10.1080/01490450903232165
775 Cabrol, L., Thalasso, F., Gandois, L., Sepulveda-Jauregui, A., Martinez-Cruz, K., Teisserenc, R., …
776 Barret, M. (2020). Anaerobic oxidation of methane and associated microbiome in anoxic water
777 of Northwestern Siberian lakes. *Science of the Total Environment*, *736*, 139588.
778 https://doi.org/10.1016/j.scitotenv.2020.139588
779 Callahan, B. J., McMurdie, P. J., Rosen, M. J., Han, A. W., Johnson, A. J. A., & Holmes, S. P. (2016).
780 DADA2: High-resolution sample inference from Illumina amplicon data. *Nature Methods*, *13*(7),
781 581–583. https://doi.org/10.1038/nmeth.3869
782 Chan, C. S., Emerson, D., & Luther, G. W. (2016). The role of microaerophilic Fe-oxidizing micro-
783 organisms in producing banded iron formations. *Geobiology*, *14*(5), 509–528.
784 https://doi.org/10.1111/gbi.12192
785 Colombo, C., Palumbo, G., He, J. Z., Pinton, R., & Cesco, S. (2014). Review on iron availability in
786 soil: Interaction of Fe minerals, plants, and microbes. In *Journal of Soils and Sediments* (Vol. 14,
787 Issue 3, pp. 538–548). https://doi.org/10.1007/s11368-013-0814-z
788 Cornell, R. M., Schwertmann, U., Bodenkunde, L., Universität, T., & Introduction, I. (1996). *The Iron*
789 *Oxides : Structure , Properties , Reactions , Occurrence and Uses Contents :* 533–559.
790 Davis, N. M., Proctor, Di. M., Holmes, S. P., Relman, D. A., & Callahan, B. J. (2018). Simple
791 statistical identification and removal of contaminant sequences in marker-gene and
792 metagenomics data. *Microbiome*, *6*(1), 1–14. https://doi.org/10.1186/s40168-018-0605-2
793 de Vet, W. W. J. M., Dinkla, I. J. T., Rietveld, L. C., & van Loosdrecht, M. C. M. (2011). Biological
794 iron oxidation by Gallionella spp. in drinking water production under fully aerated conditions.
795 *Water Research*, *45*(17), 5389–5398. https://doi.org/10.1016/j.watres.2011.07.028
796 Dold, B., Gonzalez-Toril, E., Aguilera, A., Lopez-Pamo, E., Cisternas, M. E., Bucchi, F., & Amils, R.
797 (2013). Acid Rock Drainage and Rock Weathering in Antarctica: Important Sources for Iron
798 Cycling in the Southern Ocean. *Environmental Science & Technology*, *47*(12), 6129–6136.
799 https://doi.org/10.1021/es305141b

800 Dong, L., Chen, M., Liu, C., Lv, Y., Wang, X., Lei, Q., Tong, H. (2024). Microbe interactions drive
801 the formation of floating iron films in circumneutral wetlands. *Science of the Total Environment*,
802 *906*(October 2023), 167711. https://doi.org/10.1016/j.scitotenv.2023.167711
803 Dubinsky, E. A., Silver, W. L., & Firestone, M. K. (2010). Tropical forest soil microbial communities
804 couple iron and carbon biogeochemistry. *Ecology*, *91*(9), 2604–2612. https://doi.org/10.1890/09-
805 1365.1
806 Duckworth, O. W., Holmström, S. J. M., Peña, J., & Sposito, G. (2009). Biogeochemistry of iron
807 oxidation in a circumneutral freshwater habitat. *Chemical Geology*, *260*(3–4), 149–158.
808 https://doi.org/10.1016/j.chemgeo.2008.08.027
809 Emerson, D. (2012). Biogeochemistry and microbiology of microaerobic Fe(II) oxidation.
810 *Biochemical Society Transactions*, *40*(6), 1211–1216. https://doi.org/10.1042/BST20120154
811 Emerson, D., Fleming, E. J., & McBeth, J. M. (2010). Iron-Oxidizing Bacteria: An Environmental
812 and Genomic Perspective. *Annual Review of Microbiology*, *64*(1), 561–583.
813 https://doi.org/10.1146/annurev.micro.112408.134208
814 Emerson, D., & Revsbech, N. P. (1994). Investigation of an iron-oxidizing microbial mat community
815 located near Aarhus, Denmark: Field studies. *Applied and Environmental Microbiology*, *60*(11),
816 4022–4031. https://doi.org/10.1128/aem.60.11.4022-4031.1994
817 Fabisch, M., Beulig, F., Akob, D. M., & Küsel, K. (2013). Surprising abundance of Gallionella-
818 related iron oxidizers in creek sediments at pH 4.4 or at high heavy metal concentrations.
819 *Frontiers in Microbiology*, *4*(DEC), 1–12. https://doi.org/10.3389/fmicb.2013.00390
820 Fan, Y. Y., Li, B. B., Yang, Z. C., Cheng, Y. Y., Liu, D. F., & Yu, H. Q. (2018). Abundance and
821 diversity of iron reducing bacteria communities in the sediments of a heavily polluted freshwater
822 lake. *Applied Microbiology and Biotechnology*, *102*(24), 10791–10801.
823 https://doi.org/10.1007/s00253-018-9443-1
824 Feder, F., Trolard, F., Bourrié, G., & Klingelhöfer, G. (2018). Quantitative estimation of fougerite
825 green rust in soils and sediments by citrate—bicarbonate kinetic extractions. *Soil Systems*, *2*(4),
826 1–13. https://doi.org/10.3390/soilsystems2040054
827 Folks, H. C., & Riecken, F. F. (1956). Physical and Chemical Properties of Some Iowa Soil Profiles
828 with Clay-Iron Bands. *Soil Science Society of America Journal*, Vol. 20, pp. 575–580.
829 https://doi.org/10.2136/sssaj1956.03615995002000040030x
830 Fox, G. A., Purvis, R. A., & Penn, C. J. (2016). Streambanks: A net source of sediment and
831 phosphorus to streams and rivers. *Journal of Environmental Management*, *181*, 602–614.
832 https://doi.org/10.1016/j.jenvman.2016.06.071
833 Gentry, L. E., David, M. B., Royer, T. V., Mitchell, C. A., & Starks, K. M. (2007). Phosphorus
834 Transport Pathways to Streams in Tile-Drained Agricultural Watersheds. *Journal of*
835 *Environmental Quality*, *36*(2), 408–415. https://doi.org/10.2134/jeq2006.0098
836 Grathoff, G. H., Baham, J. E., Easterly, H. R., Gassman, P., & Hugo, R. C. (2007). Mixed-valent Fe
837 films ('schwimmeisen') on the surface of reduced ephemeral pools. *Clays and Clay Minerals*,
838 *55*(6), 635–643. https://doi.org/10.1346/CCMN.2007.0550610
839 Hoagland, B., Navarre-Sitchler, A., Cowie, R., & Singha, K. (2020). Groundwater–Stream
840 Connectivity Mediates Metal(loid) Geochemistry in the Hyporheic Zone of Streams Impacted by
841 Historic Mining and Acid Rock Drainage. *Frontiers in Water*, *2*(December), 1–25.
842 https://doi.org/10.3389/frwa.2020.600409
843 Hoagland, B., Rasmussen, K. L., Singha, K., Spear, J. R., & Navarre-Sitchler, A. (2024). Metal-oxide
844 precipitation influences microbiome structure in hyporheic zones receiving acid rock drainage.
845 *Applied and Environmental Microbiology*, *90*(3). https://doi.org/10.1128/aem.01987-23

Janney, D. E., Cowley, J. M., & Buseck, P. R. (2000). Transmission electron microscopy of synthetic 2- and 6-line ferrihydrite. *Clays and Clay Minerals*, *48*(1), 111–119. https://doi.org/10.1346/CCMN.2000.0480114

Kappler, A., Bryce, C., Mansor, M., Lueder, U., Byrne, J. M., & Swanner, E. D. (2021). An evolving view on biogeochemical cycling of iron. *Nature Reviews Microbiology*, *19*(6), 360–374. https://doi.org/10.1038/s41579-020-00502-7

Kleja, D. B., van Schaik, J. W. J., Persson, I., & Gustafsson, J. P. (2012). Characterization of iron in floating surface films of some natural waters using EXAFS. *Chemical Geology*, *326–327*, 19–26. https://doi.org/10.1016/j.chemgeo.2012.06.012

Kozich, J. J., Westcott, S. L., Baxter, N. T., Highlander, S. K., & Schloss, P. D. (2013). Development of a dual-index sequencing strategy and curation pipeline for analyzing amplicon sequence data on the miseq illumina sequencing platform. *Applied and Environmental Microbiology*, *79*(17), 5112–5120. https://doi.org/10.1128/AEM.01043-13

Kozubal, M., Macur, R. E., Korf, S., Taylor, W. P., Ackerman, G. G., Nagy, A., & Inskeep, W. P. (2008). Isolation and distribution of a novel iron-oxidizing crenarchaeon from acidic geothermal springs in Yellowstone National Park. *Applied and Environmental Microbiology*, *74*(4), 942–949. https://doi.org/10.1128/AEM.01200-07

Kreiling, R. M., Bartsch, L. A., Perner, P. M., Hlavacek, E. J., & Christensen, V. G. (2021). Riparian Forest Cover Modulates Phosphorus Storage and Nitrogen Cycling in Agricultural Stream Sediments. *Environmental Management*, *68*(2), 279–293. https://doi.org/10.1007/s00267-021-01484-9

Lambrecht, N., Katsev, S., Wittkop, C., Hall, S. J., Sheik, C. S., Picard, A., Swanner, E. D. (2020). Biogeochemical and physical controls on methane fluxes from two ferruginous meromictic lakes. *Geobiology*, *18*(1), 54–69. https://doi.org/10.1111/gbi.12365

Lautz, L. K., & Fanelli, R. M. (2008). Seasonal biogeochemical hotspots in the streambed around restoration structures. *Biogeochemistry*, *91*(1), 85–104. https://doi.org/10.1007/s10533-008-9235-2

Lautz, L. K., Siegel, D. I., & Bauer, R. L. (2006). Impact of debris dams on hyporheic interaction along a semi-arid stream. *Hydrological Processes*, *20*(1), 183–196. https://doi.org/10.1002/hyp.5910

Lawrence, J. E., Skold, M. E., Hussain, F. A., Silverman, D. R., Resh, V. H., Sedlak, D. L., … McCray, J. E. (2013). Hyporheic zone in urban streams: A review and opportunities for enhancing water quality and improving aquatic habitat by active management. *Environmental Engineering Science*, *30*(8), 480–501. https://doi.org/10.1089/ees.2012.0235

Lefler, F. W., Berthold, D. E., & Laughinghouse, H. D. (2023). Cyanoseq: A database of cyanobacterial 16S rRNA gene sequences with curated taxonomy. *Journal of Phycology*, *59*(3), 470–480. https://doi.org/10.1111/jpy.13335

Leopold, R. (2010). *The Iowa State-Wide Trace Element Soil Sampling Project : Design and Implementation*. (June), 1–78.

Lovley, D. R. (1987). Organic matter mineralization with the reduction of ferric iron: A review. *Geomicrobiology Journal*, *5*(3–4), 375–399. https://doi.org/10.1080/01490458709385975

Melton, E. D., Swanner, E. D., Behrens, S., Schmidt, C., & Kappler, A. (2014). The interplay of microbially mediated and abiotic reactions in the biogeochemical Fe cycle. *Nature Reviews Microbiology*, *12*(12), 797–808. https://doi.org/10.1038/nrmicro3347

Méndez-García, C., Peláez, A. I., Mesa, V., Sánchez, J., Golyshina, O. V., & Ferrer, M. (2015). Microbial diversity and metabolic networks in acid mine drainage habitats. *Frontiers in Microbiology*, *6*(MAY), 1–17. https://doi.org/10.3389/fmicb.2015.00475

Mori, J. F., Neu, T. R., Lu, S., Händel, M., Totsche, K. U., & Küsel, K. (2015). Iron encrustations on filamentous algae colonized by Gallionella-related bacteria in a metal-polluted freshwater stream. *Biogeosciences*, *12*(18), 5277–5289. https://doi.org/10.5194/bg-12-5277-2015

Murphy, J., & Riley, J. P. (1962). A modified single solution method for the determination of phosphate in natural waters. *Analytica Chimica Acta*, *27*(C), 31–36. https://doi.org/10.1016/S0003-2670(00)88444-5

Neidhardt, H., Schoeckle, D., Schleinitz, A., Eiche, E., Berner, Z., Tram, P. T. K., … Berg, M. (2018). Biogeochemical phosphorus cycling in groundwater ecosystems – Insights from South and Southeast Asian floodplain and delta aquifers. *Science of the Total Environment*, *644*, 1357–1370. https://doi.org/10.1016/j.scitotenv.2018.07.056

Perkins, R. B., Gray, Z. N., Grathoff, G., & Hugo, R. (2016). Characterization of natural and synthetic floating iron surface films and their associated waters. *Chemical Geology*, *444*, 16–26. https://doi.org/10.1016/j.chemgeo.2016.09.027

Pierson, B. K., & Parenteau, M. N. (2000). Phototrophs in high iron microbial mats: Microstructure of mats in iron-depositing hot springs. *FEMS Microbiology Ecology*, *32*(3), 181–196. https://doi.org/10.1016/S0168-6496(00)00018-0

Rentz, J. A., Kraiya, C., Luther, G. W., & Emerson, D. (2007). Control of ferrous iron oxidation within circumneutral microbial iron mats by cellular activity and autocatalysis. *Environmental Science and Technology*, *41*(17), 6084–6089. https://doi.org/10.1021/es062203e

Rentz, J. A., Turner, I. P., & Ullman, J. L. (2009). Removal of phosphorus from solution using biogenic iron oxides. *Water Research*, *43*(7), 2029–2035. https://doi.org/10.1016/j.watres.2009.02.021

Rivett, M. O., Ellis, P. A., & Mackay, R. (2011). Urban groundwater baseflow influence upon inorganic river-water quality: The River Tame headwaters catchment in the City of Birmingham, UK. *Journal of Hydrology*, *400*(1–2), 206–222. https://doi.org/10.1016/j.jhydrol.2011.01.036

Roden, E. E., McBeth, J. M., Blöthe, M., Percak-Dennett, E. M., Fleming, E. J., Holyoke, R. R., Luther, G. W., Emerson, D., & Schieber, J. (2012). The microbial ferrous wheel in a neutral pH groundwater seep. *Frontiers in Microbiology*, *3*(MAY), 1–18. https://doi.org/10.3389/fmicb.2012.00172

Rosenberg, B. D., & Schroth, A. W. (2017). Coupling of reactive riverine phosphorus and iron species during hot transport moments: impacts of land cover and seasonality. *Biogeochemistry*, *132*(1–2), 103–122. https://doi.org/10.1007/s10533-016-0290-9

Rutherford, J. S. (2005). Crystal Structure. *Encyclopedia of Condensed Matter Physics*, 289–294. https://doi.org/10.1016/B0-12-369401-9/00686-0

Sánchez-España, J., Ilin, A. M., Yusta, I., van der Graaf, C. M., & Sánchez-Andrea, I. (2023). Fe(III) Biomineralization in the Surface Microlayer of Acid Mine Waters Catalyzed by Neustonic Fe(II)-Oxidizing Microorganisms. *Minerals*, *13*(4). https://doi.org/10.3390/min13040508

Sarkkola, S., Nieminen, M., Koivusalo, H., Laurén, A., Kortelainen, P., Mattsson, T., … Finér, L. (2013). Iron concentrations are increasing in surface waters from forested headwater catchments in eastern Finland. *Science of The Total Environment*, *463–464*, 683–689. https://doi.org/https://doi.org/10.1016/j.scitotenv.2013.06.072

Schilling, K. E., Kim, S., Jones, C. S., & Wolter, C. F. (2017). Orthophosphorus Contributions to Total Phosphorus Concentrations and Loads in Iowa Agricultural Watersheds . *Journal of Environmental Quality*, *46*(4), 828–835. https://doi.org/10.2134/jeq2017.01.0015

Schwertmann, U.; Cornell, R.M.: Iron oxides in the Laboratory; Wiley VCH 2000

Shimizu, M., Zhou, J., Schröder, C., Obst, M., Kappler, A., & Borch, T. (2013). Dissimilatory reduction and transformation of ferrihydrite-humic acid coprecipitates. *Environmental Science and Technology*, *47*(23), 13375–13384. https://doi.org/10.1021/es402812j

Sobolev, D., & Roden, E. E. (2002). Evidence for rapid microscale bacterial redox cycling of iron in circumneutral environments. *Antonie van Leeuwenhoek, International Journal of General and Molecular Microbiology*, *81*(1–4), 587–597. https://doi.org/10.1023/A:1020569908536

Soto-Varela, F., Rodríguez-Blanco, M. L., Taboada-Castro, M. M., & Taboada-Castro, M. T. (2015). Metals discharged during different flow conditions from a mixed agricultural-forest catchment (NW Spain). *Hydrological Processes*, *29*(6), 1644–1655. https://doi.org/10.1002/hyp.10282

St Clair, B., Pottenger, J., Debes, R., Hanselmann, K., & Shock, E. (2019). Distinguishing Biotic and Abiotic Iron Oxidation at Low Temperatures. *ACS Earth and Space Chemistry*, *3*(6), 905–921. https://doi.org/10.1021/acsearthspacechem.9b00016

Stookey, L. L. (1970). Ferrozine-A New Spectrophotometric Reagent for Iron. *Analytical Chemistry*, *42*(7), 779–781. https://doi.org/10.1021/ac60289a016

Tobler, N. B., Hofstetter, T. B., Straub, K. L., Fontana, D., & Schwarzenbach, R. P. (2007). Iron-mediated microbial oxidation and abiotic reduction of organic contaminants under anoxic conditions. *Environmental Science and Technology*, *41*(22), 7765–7772. https://doi.org/10.1021/es071128k

Toner, B. M., Santelli, C. M., Marcus, M. A., Wirth, R., Chan, C. S., McCollom, T., … Edwards, K. J. (2009). Biogenic iron oxyhydroxide formation at mid-ocean ridge hydrothermal vents: Juan de Fuca Ridge. *Geochimica et Cosmochimica Acta*, *73*(2), 388–403. https://doi.org/10.1016/j.gca.2008.09.035

Trolard, F., & Bourrié, G. (2006). Structure of fougerite and green rusts and a thermodynamic model for their stabilities. *Journal of Geochemical Exploration*, *88*(1-3 SPEC. ISS.), 249–251. https://doi.org/10.1016/j.gexplo.2005.08.048

USGS. (2022). *StreamStats Report*. 1–13.

Usman, M., Hanna, K., Abdelmoula, M., Zegeye, A., Faure, P., & Ruby, C. (2012). Formation of green rust via mineralogical transformation of ferric oxides (ferrihydrite, goethite and hematite). *Applied Clay Science*, *64*, 38–43. https://doi.org/10.1016/j.clay.2011.10.008

Viollier, E., Inglett, P. W., Hunter, K., Roychoudhury, A. N., and Van Cappellen, P. (2000). The ferrozine method revisited: Fe(II)/Fe(III) determination in natural waters. Appl. Geochemistry 15, 785–790. doi: 10.1016/S0883-2927(99)00097-9

Williams, M. R., Wessel, B. M., & Filoso, S. (2016). Sources of iron (Fe) and factors regulating the development of flocculate from Fe-oxidizing bacteria in regenerative streamwater conveyance structures. *Ecological Engineering*, *95*, 723–737. https://doi.org/10.1016/j.ecoleng.2016.06.120

Wu, C. Y., Zhuang, L., Zhou, S. G., Li, F. B., & Li, X. M. (2010). Fe(III)-enhanced anaerobic transformation of 2,4-dichlorophenoxyacetic acid by an iron-reducing bacterium Comamonas koreensis CY01. *FEMS Microbiology Ecology*, *71*(1), 106–113. https://doi.org/10.1111/j.1574-6941.2009.00796.x

Yang, C., Zhang, Y. K., Liu, Y., Yang, X., & Liu, C. (2018). Model-Based Analysis of the Effects of Dam-Induced River Water and Groundwater Interactions on Hydro-Biogeochemical

Transformation of Redox Sensitive Contaminants in a Hyporheic Zone. *Water Resources Research*, *54*(9), 5973–5985. https://doi.org/10.1029/2018WR023286

Zegeye, A., Bonneville, S., Benning, L. G., Sturm, A., Fowle, D. A., Jones, C. A., … Poulton, S. W. (2012). Green rust formation controls nutrient availability in a ferruginous water column. *Geology*, *40*(7), 599–602. https://doi.org/10.1130/G32959.1

Zhang, X., Müller, M., Jiang, S., Wu, Y., Zhu, X., Mujahid, A., Zhu, Z., Fakharuddin Muhamad, M., Sien Aun Sia, E., Holt Ajon Jang, F., & Zhang, J. (2020). Distribution and flux of dissolved iron in the peatland-draining rivers and estuaries of Sarawak, Malaysian Borneo. *Biogeosciences*, *17*(7), 1805–1819. https://doi.org/10.5194/bg-17-1805-2020

Supplemental Information:

Piezometer Locations

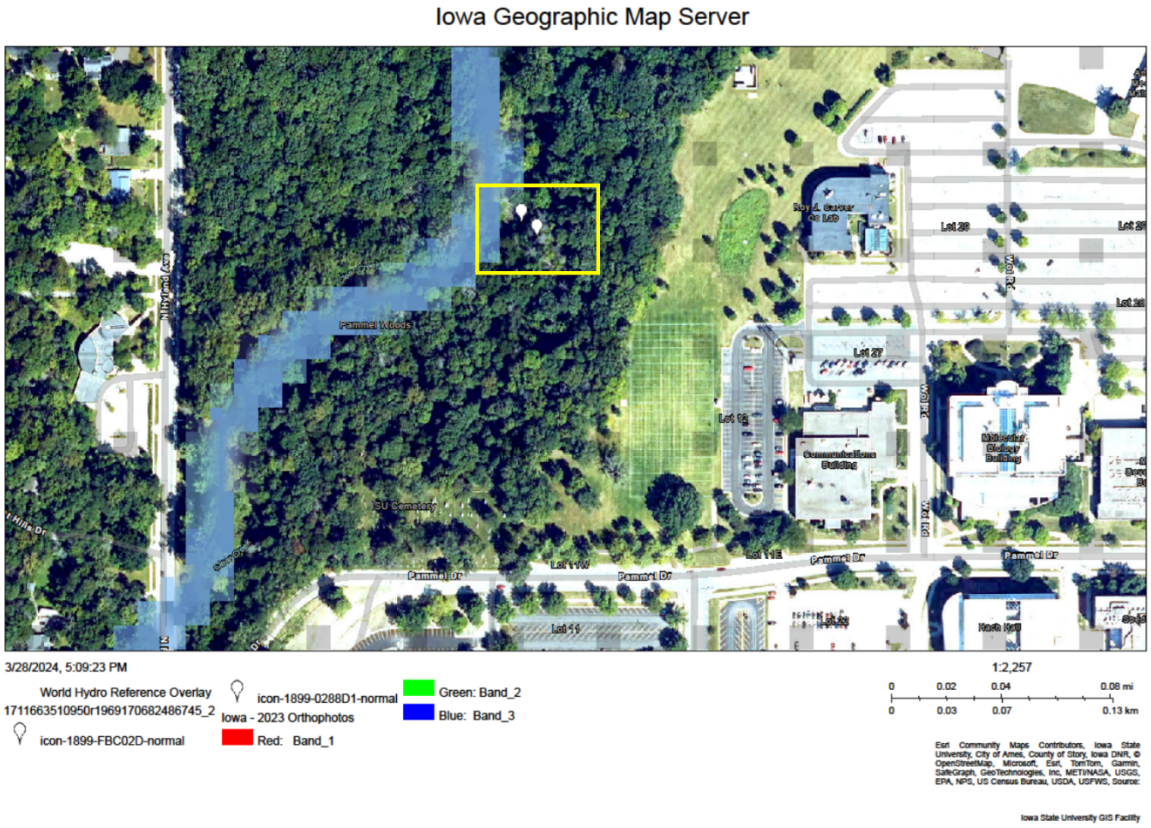

Supplemental Figure 1: Location of piezometers indicated by the white markers. These are located around the midpoint of the sampling sites. Shaded in blue is Clear Creek.

Alpha diversity measurements:

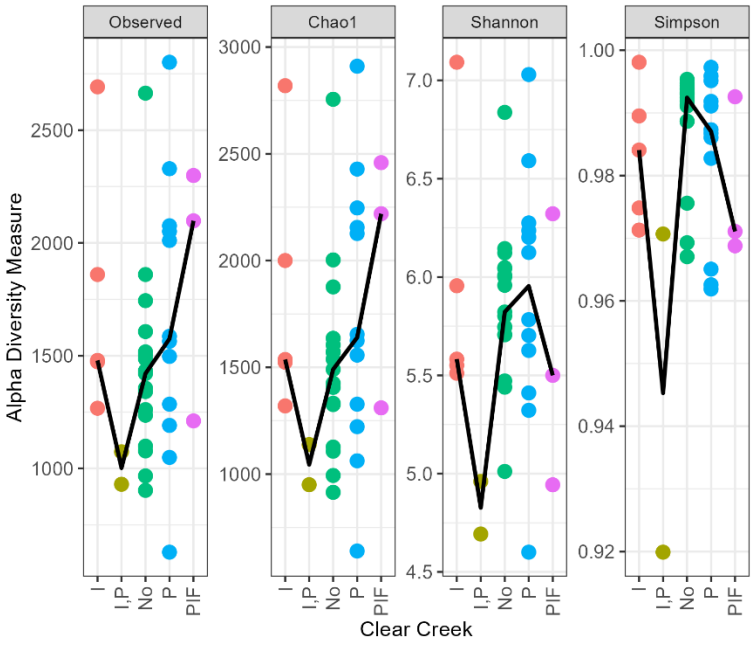

Supplemental Figure 2: Alpha diversity measured by Shannon, Simpson, and Chao1 indices estimated between different iron types of Clear Creek for 16S rRNA. X-axis labels: No: no iron present, I: iridescent, P: iron precipitates, I,P: both iridescence and precipitates, and PIF: all three iron types. Black line indicates median values through iron types.

Microbial Analysis:

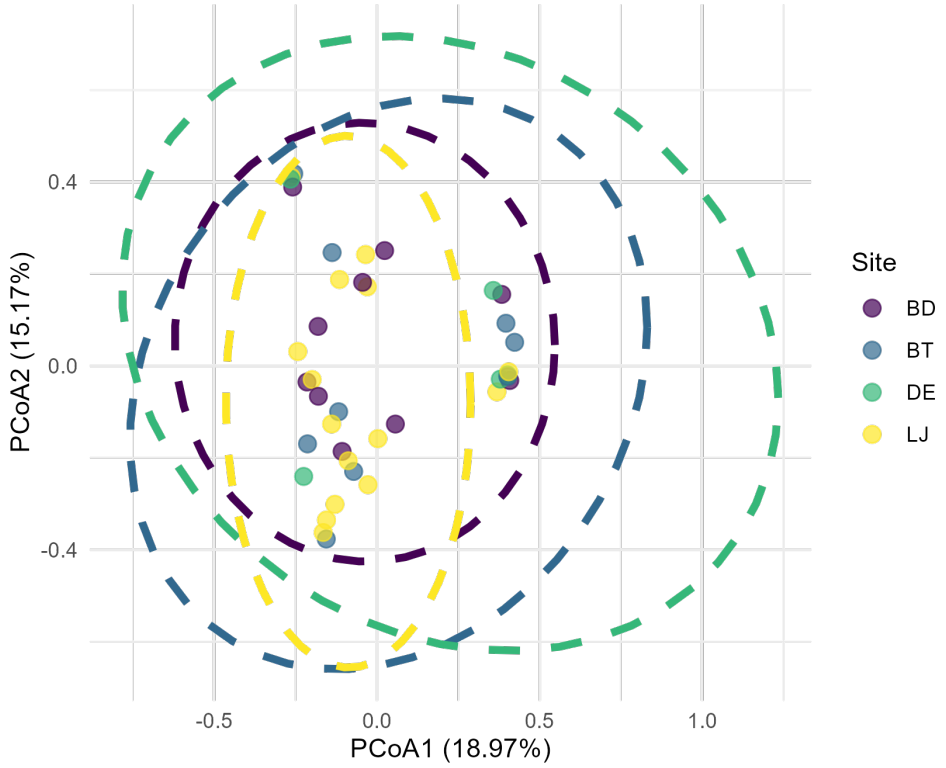

Supplemental Figure 3: Principal Coordinates Analyses conducted by contrast based on Bray-Curtis distance highlighted by site. Ellipses are plotted with a 95% confidence interval and plotted with the percentage of variability on the axis. No statistical difference was determined from a Permanova.

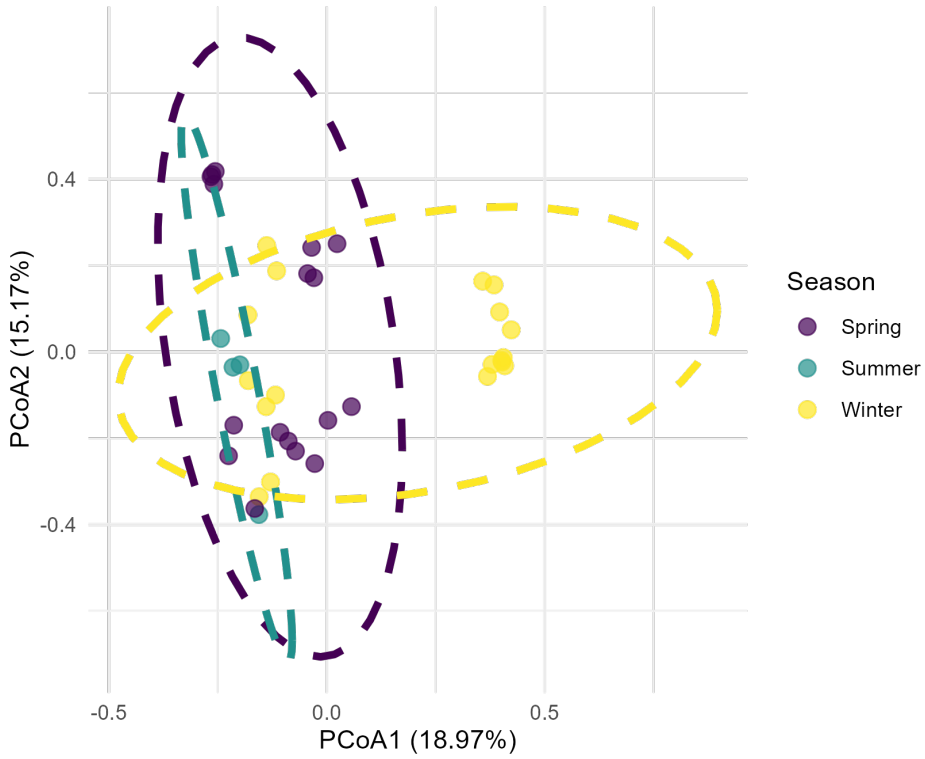

Supplemental Figure 4: Principal Coordinates Analyses conducted by contrast based on Bray-Curtis distance highlighted by season. Ellipses are plotted with a 95% confidence interval and plotted with the percentage of variability on the axis. Permanova found a significant statistical difference between seasons (<0.001).

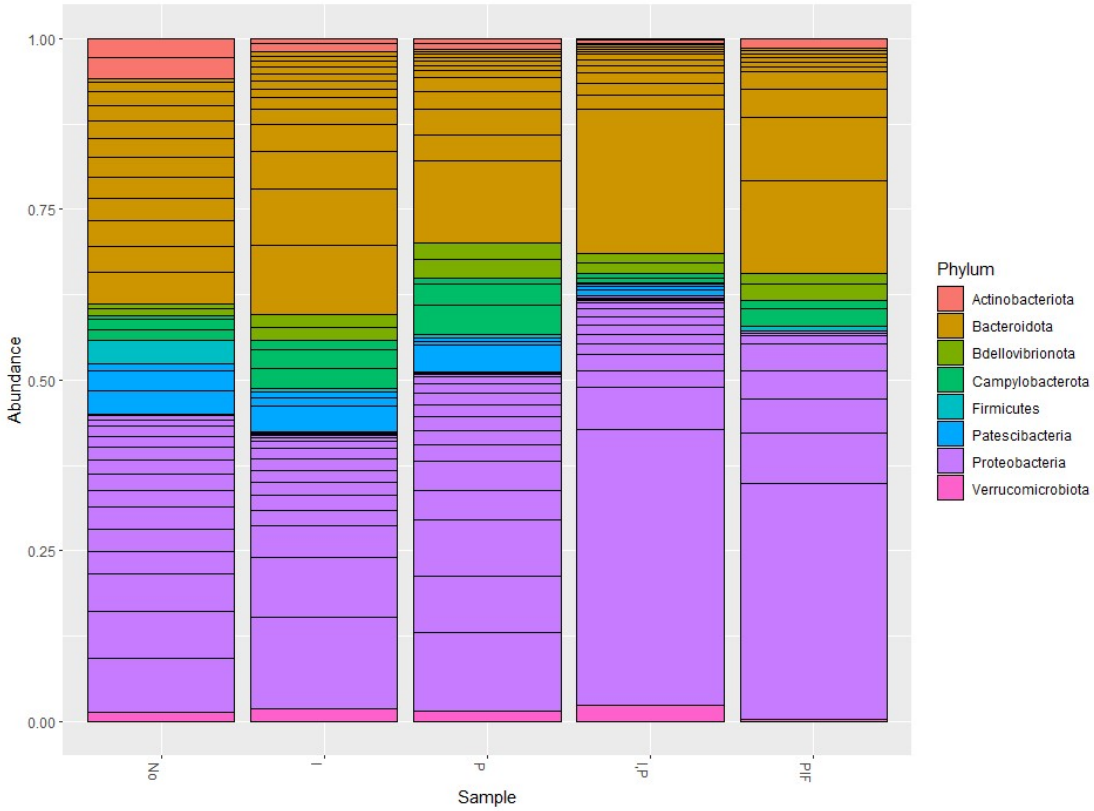

Supplemental Figure 5: 16S abundance at the Phylum level based on iron mineralization types.

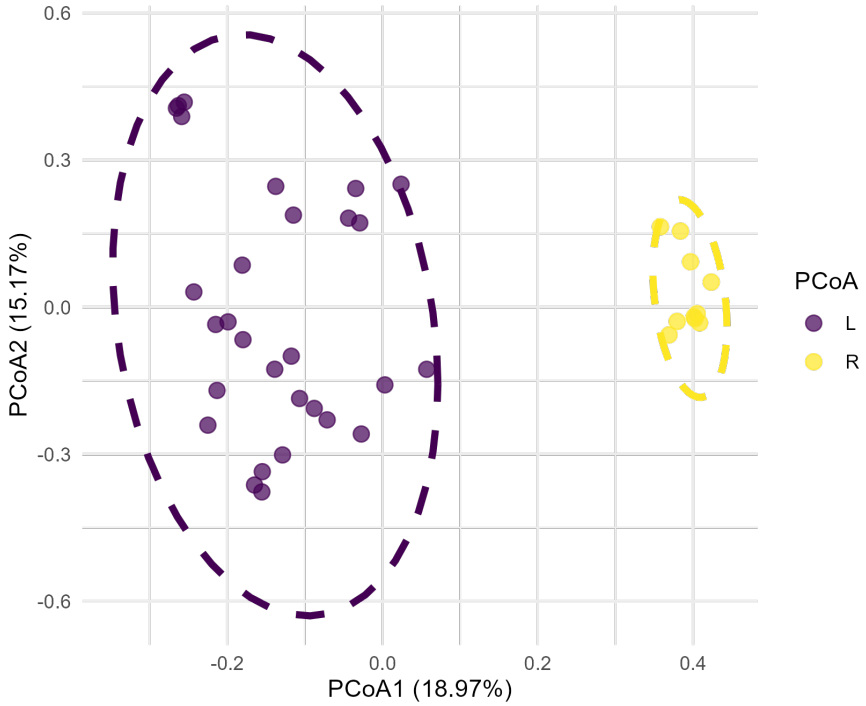

Supplemental Figure 6: Principal Coordinates Analyses conducted by contrast based on Bray-Curtis distance highlighted by samples with clustering on left and right. Ellipses are plotted with a 95% confidence interval and plotted with the percentage of variability on the axis. Permanova found a significant statistical difference between left and right samples (<0.001).

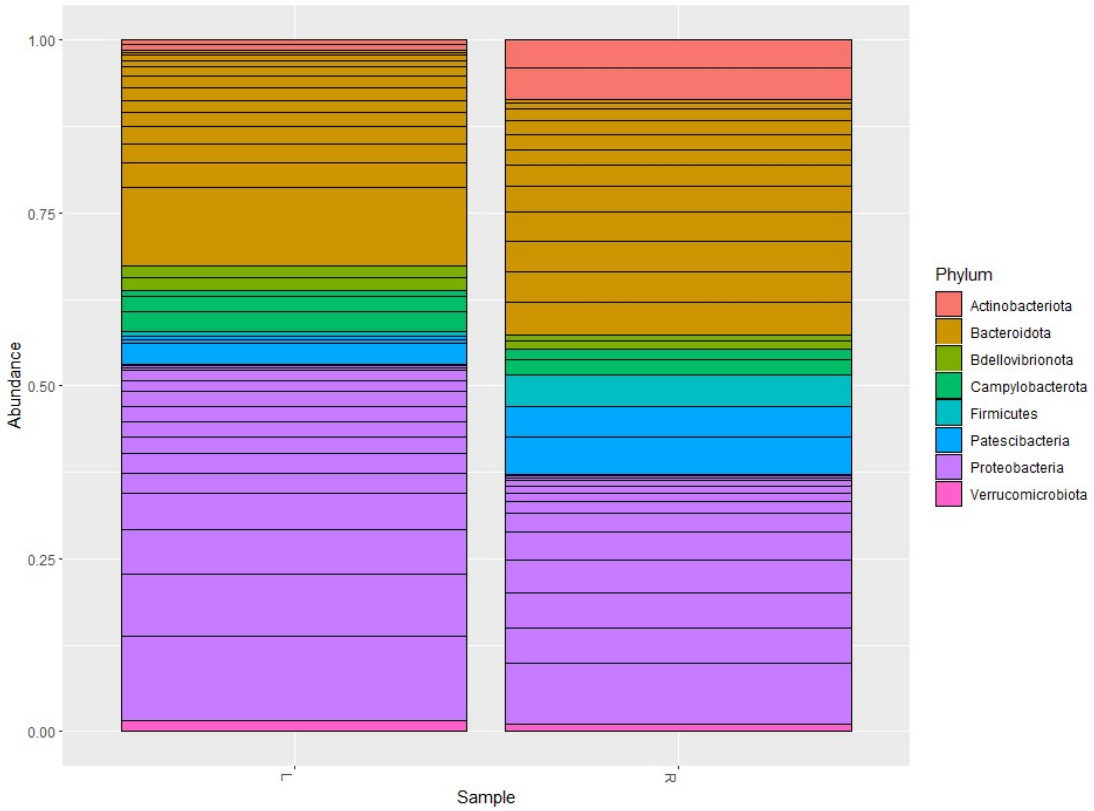

Supplemental Figure 7: Top 30 abundance based on Phylum level in Left and Right Clusters from PCoA plot.

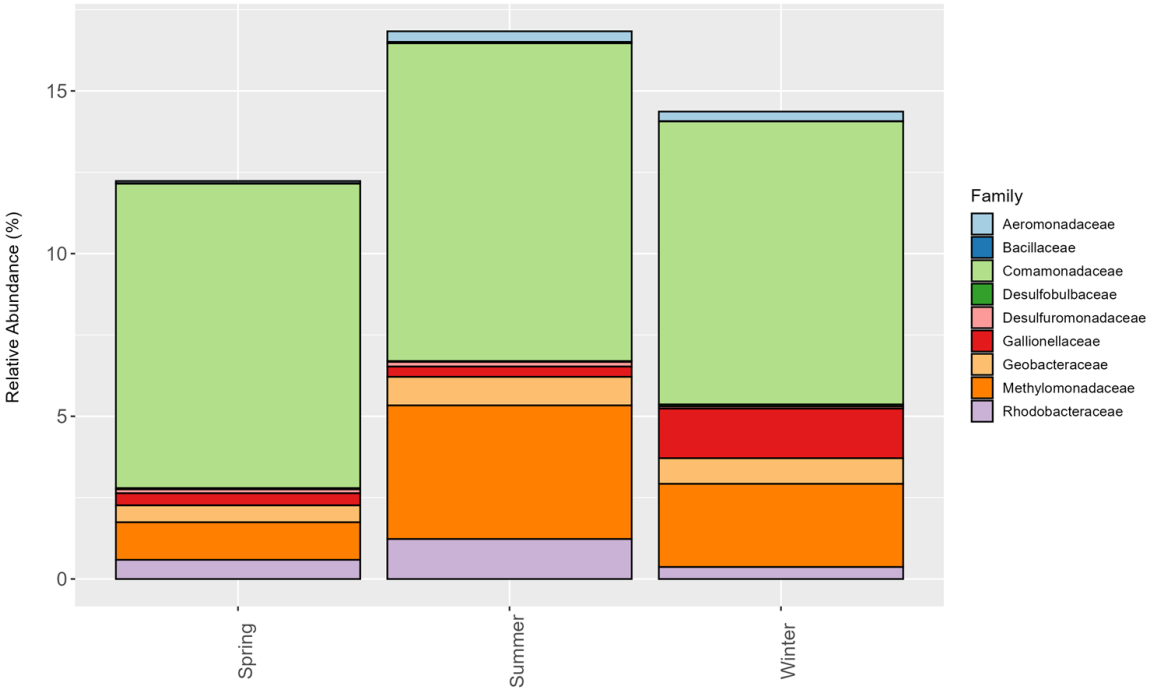

Supplemental Figure 8: Relative abundance at the Family level of putative iron cyclers + methane-oxidizing bacteria based on season.

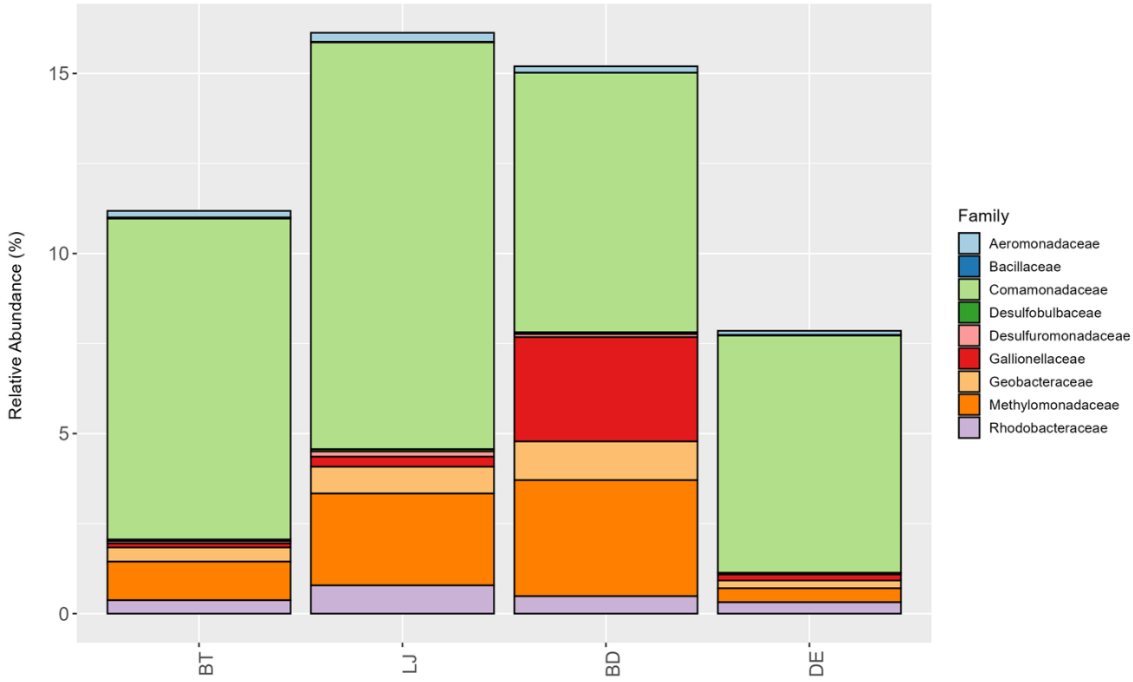

Supplemental Figure 9: Relative abundance at the Family level of putative iron cyclers + methane-oxidizing bacteria at the different sample sites.

Low and High Loss Calibration EELS:

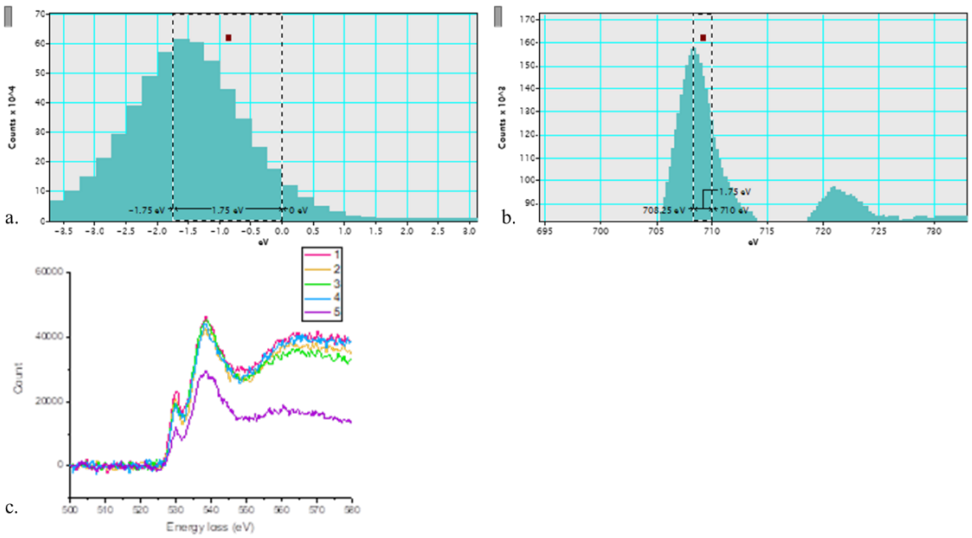

Supplemental Figure 10: a and b) Energy calibration of EELS. a) Prior to EELS analysis on sample, a zero loss peak was acquired, showing a -1.75 eV shift from 0 eV. b) The -1.75 eV shift was applied to the collected high-loss data. c) O-K edge for 5 sample areas of interest from Figures 8 & 9.